The role of Ir decoration in activating multi-scale fractal surface in porous Ni for the oxygen evolution reaction

Hao, M., Assresahegn, B. D., Abdellah, A., Miner, L., Al Hejami, A., Zaker, N., . . . Guay, D.

2023

Citation for this paper:

Hao, M., Assresahegn, B. D., Abdellah, A., Miner, L., Al Hejami, A., Zaker, N., . . . Guay, D. (2023). The role of Ir decoration in activating multi-scale fractal surface in porous Ni for the oxygen evolution reaction. *ACS Catalysis, 13*(1), 1726-1739. https://doi.org/10.1021/acscatal.2c05349 doi: 10.1021/acscatal.2c05349

The role of Ir decoration in activating multi-scale fractal surface in porous Ni for the oxygen evolution reaction

Minghui Hao[1], Birhanu Desalegn Assresahegn[1], Ahmed Abdellah[2], Lukas Miner[4],
Ahmed Al Hejami[4], Nafiseh Zaker[3], Julie Gaudet[1], Lionel Roué[1],
Gianluigi A. Botton[3], Diane Beauchemin[4], Drew C. Higgins[2]
Steven Thorpe[5], David A. Harrington[6], Daniel Guay[1] *

[1] Institut national de la recherche scientifique (INRS), Centre Énergie, Matériaux Télécommunications, Varennes, QC J3X 1P7, Canada.

[2] Department of Chemical Engineering, McMaster University, Hamilton, Ontario L8S 4L7, Canada

[3] Department of Materials Science and Engineering, McMaster University, 1280 Main Street West Hamilton, ON L8S 4L7, Canada.

[4] Department of Chemistry, 90 Bader Lane, Queen's University, Kingston, ON K7L 3N6, Canada.

[5] Department of Materials Science and Engineering, University of Toronto, 184 College Street, Toronto, ON M5S 3E4 Canada.

[6] Department of Chemistry, University of Victoria, Victoria, BC V8W 2Y2, Canada.

Keywords: Gas-evolving reaction; Gas bubbles; Wettability; Porous electrode; Impedance; Ir incorporation; Alkaline water electrolysis

* Corresponding author: daniel.guay@inrs.ca

Abstract

Interfacial engineering of electrocatalysts is a pivotal approach for promoting the energy conversion efficiency of water electrolysis systems. Anchoring clusters or even single atoms of a foreign element on the surface of a support, usually 3D structured, can alter its local electronic structure leading to superior electrocatalytic activity. Herein, we report a method to decorate a 3D fractal Ni electrode with Ir atoms via a galvanic displacement reaction. The resulting electrode has a very low Ir loading of 1.6 μmole cm_{geo}^{-2}, with iridium atoms present as 4-5 nm diameter nanoclusters on the electrode surface. The activity for the electrochemical oxygen evolution reaction (OER) of the 3D fractal Ni electrode was improved by decoration with Ir, resulting in an overpotential of 195 mV at 10 mA cm^{-2} and a Tafel slope of 44 mV dec^{-1}. Apart from increasing the electrocatalytic activity for the OER due to the very presence of more active iridium atoms, the galvanic displacement reaction resulted in a factor 8-10 increase of the electrochemically active surface area due to the creation/activation of a secondary pore structure that contributes also to the better electrocatalytic performance of the resulting electrode. Using *operando* acoustic emission, it is demonstrated that the galvanic displacement reaction and the presence of Ir nanoclusters have the additional effect of reducing the average O_2 bubble size formed during the OER. As a result, the blocking effect of O_2 bubbles at high current density is less drastic than on the 3D fractal Ni electrode, resulting in a less severe decrease of the electrochemically active area at large current density. All three effects contribute towards improving the OER performance of the Ir-decorated 3D fractal Ni electrode.

Introduction

A power-to-gas (P2G) system is composed of a series of technologies that convert instantaneous energies, such as renewable energy or the surplus energy in power grids, into stable gas fuel [1]. Such a system offers a promising prospect for solving the energy crisis that human society is facing. Water electrolysis for the sustainable production of hydrogen is a core component of the whole P2G conversion system. Water electrolysis involves two gas evolution reactions: the hydrogen evolution reaction (HER) and the oxygen evolution reaction (OER). Due to the sluggishness of the OER kinetics, which limits the overall efficiency of the water electrolysis process, improvement of the existing OER electrocatalysts is required.

Currently, state-of-the-art electrocatalysts for the OER in acidic solutions are IrO_2 and RuO_2 [2–5]. However, ruthenium and iridium are rare metals that are prohibitively expensive, which slows down the large-scale deployment of acid-based electrolyzers. In contrast, alkaline-based water electrolysis imposes far fewer constraints on the choice of materials, and nickel has been widely studied for the OER in alkaline media due to its low cost and long-term stability. However, several studies have shown that pure Ni is a poor electrocatalyst for the OER unless it is doped/mixed with other elements [6,7]. Thus, recent studies have focused on strategies to increase the electrocatalytic activity of Ni-based materials by doping/mixing it with non-noble metals and elements, including NiFe layered double hydroxides (LDHs), NiS_x, Ni_xP_y, and $NiSe_x$, which have shown good performance for the OER in alkaline water electrolysis [8]. Another strategy consists in incorporating minimal amounts of a noble metal, like Ir, to modify the electronic structure of Ni and increase the performance of the resulting materials for the OER [9]. Accordingly, several systems and methods of preparation have been investigated, including IrNi bimetallic nanoparticles [10–13], $IrNi_x$-IrO_x core-shell nanoparticles [14,15], Ir-Ni binary oxide [16,17], thermally prepared Ir-Ni mixed oxide thin films [18], IrO_2 shell/Ir-Ni core particles [19,20], Ni deposits on polycrystalline and oriented iridium surfaces [21], pulsed-electrodeposition of Ir-Ni oxides [22], and deposition of isolated iridium atoms on a NiO matrix [23].

Of all the preparation methods that have been investigated, iridium deposition by the galvanic displacement reaction is of particular interest because it is simple and allows fine control of the amount of iridium atoms deposited [19,24,25]. Also, it enables iridium atoms to be localized on the electrode surface, where their contribution will have the greatest impact on improving the performance for the OER. The galvanic displacement reaction enables decoupling the fabrication of the porous Ni substrate from its activation, and thus optimizing its structure to maximize catalyst utilization.

It was recently shown that multi-scale fractal Ni electrodes could be prepared by hydrogen bubble template electrodeposition[26]. These 3D porous Ni electrodes have a very large electrochemically active surface area, with a roughness factor exceeding 270. Also, they are superaerophobic, with captive air bubble making a contact angle larger than 150° [26]. Indeed, having a superaerophobic 3D porous structure is critical since gas bubbles are generated during the OER. Dynamic bubble occupation on the electrode surface, and even in the internal structure of the porous electrode, can significantly reduce the accessibility of the electrolyte to the active sites, thereby increasing the overpotential of the OER and causing undesirable energy losses [27,28]. The use of electrodes that have a superaerophobic character could counteract the negative effect of gas bubble masking the catalytically active sites by reducing the departure size of gas bubbles and lowering their adhesion force. Thus, in the literature, a variety of attempts have been made to achieve passive management of gas bubbles at gas evolving electrodes by increasing their wettability and rendering them superaerophobic [26–33].

In the present study, 3D multi-fractal superaerophobic Ni electrodes were catalyzed by a small amount of iridium atoms. A galvanic displacement reaction was used to deposit iridium atoms. The Ir deposition process has unsuspected effects on the structure of the Ni electrode and the OER performance of the resulting electrode by revealing/creating a secondary pore structure not present initially, by decreasing the size of the oxygen bubbles and helping to mitigate the deleterious effect they have on reducing the electrochemically active surface area during the OER. Added to the beneficial effect of the very presence of iridium atoms, all these effects combine to increase the electrocatalytic activity for the OER.

Experimental section

Preparation of Ni DHBT electrode and deposition of Ir

The multi-scale fractal Ni electrode was prepared by dynamic hydrogen bubble electrodeposition[26]. For this, 1 cm^2 Ni rod (Sigma-Aldrich, 99.99%) or 1 cm^2 Ni plates (Alfa Aesar, Puratronic 99.9945% metal basis) were used as substrates. They were inserted into a custom-built electrochemical cell and used as substrates for the electrodeposition of a porous Ni film. The deposition was performed for 450 s at -2 A cm^{-2} in a 0.1 M $NiCl_2·6H_2O$ + 2 M NH_4Cl electrolyte. Then, samples were thoroughly rinsed with Type I Ultrapure water (Millipore Milli-Q, resistivity 18.2 MΩ cm). The prepared materials will be denoted as Ni DHBT films in the following sections. They were subsequently immersed in 0.01 M HCl or 0.001 M K_2IrCl_6 + 0.01 M HCl solution for up to 20 hours. These later samples were denoted as Ir/Ni DHBT.

Dissolution of Ni measured by inductively coupled plasma spectroscopy

Iridium atoms were deposited on the Ni electrode through the galvanic displacement reaction. This was achieved by immersion of the Ni DHBT electrode in a 0.001 M K_2IrCl_6 + 0.01 M HCl solution for different periods. The amount of Ir atoms deposited at the electrode surface and Ni atoms released to the solution were assessed through inductively coupled plasma spectroscopy (lateral-view ARCOS, SPECTRO Analytical Instruments, Kleve, Germany). For these measurements, 1 cm^2 samples were immersed in the appropriate electrolytes. The concentrations of Ni and Ir in the electrolyte following immersion for 0 to 21 hours were measured by external calibration with at least 5 standard solutions prepared in 0.01 M HCl, along with internal standardization using an argon emission line (at 404.442 nm). All calibration curves were linear, with an R^2 value of >0.9999.

Physical Characterization of Ni/DHBT and Ir/Ni DHBT films

The surface morphology of Ni DHBT and Ir/Ni DHBT films were probed by scanning electron microscopy (SEMs) using a VEGA3 TESCAN SEM and a FEI Magellan ultrahigh-resolution SEM operated between 1 keV to 2 keV incident energy for imaging. Energy dispersive X-ray (EDX) mapping was performed to assess the film compositions. X-ray diffraction (XRD) patterns were obtained using a Bruker D8 Advance X-ray diffractometer with a weighted average Cu $K_{\alpha1}$ and Cu $K_{\alpha2}$ radiation at 1.5418 Å. The data were collected in the 2θ range from 30° to 95°, the step size was 0.02 degrees, and the counting time was 2 seconds per step. High-resolution transmission electron microscopy (HRTEM) and high-angle annular dark-field scanning transmission electron microscopy (HAADF-STEM) micrographs along with energy-dispersive spectroscopy (EDS) mapping were obtained at the Canadian Centre for Electron Microscopy (CCEM) using a Talos 200X operated at 200 keV.

Electrochemical characterization

Electrochemical measurements were carried out in a custom-built electrochemical cell with a Pt mesh (Alfa Aesar, 99.9%) as the counter electrode and a saturated calomel electrode (SCE) as the reference electrode. The potentials were converted relative to the reversible hydrogen electrode (RHE) following the equation $E_{RHE} = E_{SCE} + 0.242\ \text{V} + 0.059\text{V} \times \text{pH}$. Most electrochemical measurements were performed in 1M KOH electrolyte (pH = 13.5) prepared with Type I Ultrapure water (Millipore Milli-Q, resistivity 18.2 MΩ cm) and KOH (Sigma-Aldrich, 99.99% trace metals basis).

A Solartron 1480 potentiostat was used for the electrochemical measurements, and a Solartron 1255B frequency analyzer was used for the electrochemical impedance spectroscopy (EIS) measurements. For each measurement, the uncompensated resistance, R_u, was determined at open circuit potential (OCP) by taking the high frequency intercept of the Nyquist plot measured between 0.01Hz and 200kHz.

Prior to cyclic voltammetry (CV) measurements, all samples were immersed at OCP in 1M KOH electrolyte for 15 min. Then, CV scans at a scan rate of 50 mV s^{-1} were recorded between −0.1 to 1.5 V *vs* RHE until stable CVs were obtained. Stable CVs were obtained after 50 cycles. All CVs shown in this study were recorded at 5 mV s^{-1} after the above-described procedure was applied.

Electrochemical Impedance Spectroscopy (EIS) measurements between 0.01 Hz and 200 kHz with 10 mV amplitude were conducted after a constant potential was applied to the electrode during 5 min. These conditions were sufficient for the electrode to reach a steady state current. The electrode potential was varied from 1.44 to 1.49 V in the regime of the OER.

Electrochemical impedance data were fitted using a transmission line model (TLM) and the de Levie Equation [34] (equation 1). The complex nonlinear least squares (CNLS) fitting program of Matlab® was used.

$$Z = R_u + \frac{R_\Omega}{\Lambda^{1/2}} coth\left(\Lambda^{1/2}\right) \; with \; \Lambda = i\omega c_{dl} + \frac{1}{r_{ct}} \qquad Equation\ 1$$

where c_{dl} and r_{ct} are the double-layer capacitance and charge-transfer resistance on the pore walls, respectively, R_Ω is the total solution resistance (Ω cm^2) within the pores, and R_u is the uncompensated resistance.

Acoustic Emission

Acoustic emission measurements were conducted in a custom-built three-electrode electrochemical cell, using a piezoelectric sensor (R6A, Mistras) and a detecting system (1283 USB AE Node, Mistras). A cylindrical Ni rod was used as substrate. Ni DHBT and Ir/Ni DHBT coatings were deposited on one side of the Ni rod. On the other side, the AE sensor was connected. The AE sensor was not in contact with the electrolyte. The center of the AE sensor and the working electrode were aligned on a common axis. Silicon grease and Kapton tape are applied between the Ni rod and the AE sensor to minimize the air gap and electrically isolated them from one another. Positive currents varying from 0.3 mA cm^{-2} to 6.6 mA cm^{-2} were applied on the working electrode to generate O_2 bubbles. During the OER, pulsed AE signals with an amplitude larger than 28 dB were recorded and counted as discrete AE events. Data processing of the AE events were conducted using the AEwin software (Mistras). For each AE event, the peak frequency was determined by Fourier transform in AEwin.

Surface Characterization by XPS

X-ray photoelectron spectroscopy (XPS) measurements were performed using a VG Escalab 220i-XL instrument equipped with an Al K_α source. Freshly prepared Ni and Ir/Ni DHBT films were introduced into the XPS vacuum chamber for drying overnight right after they were prepared. Also, some deposits were analyzed after their electrochemical characterization. The same procedure was followed. These samples are denoted post-EC Ni DHBT and post-EC Ir/Ni DHBT. Data fitting was performed with the CasaXPS software using Shirley background subtractions. For surface charging correction, the C 1s peak at 284.8eV was used as a reference.

Results and discussion

Physico-chemical characterization

Three-dimensional porous Ni DHBT films were electrodeposited on flat Ni substrates. Figure 1 shows that Ni DHBT films have an interconnected cauliflower-like structure with pore diameters varying between 10 and 30 µm. This unique structure results from the simultaneous electrodeposition of Ni and the formation and release of hydrogen bubbles occurring at large negative potential, typically *ca.* -4 V *vs* RHE, applied to reach a deposition current of -2 A cm^{-2}.

Deposition of minute amount of Ir atoms at the surface of Ni DHBT was performed through the galvanic replacement reaction. This was achieved through immersing of the Ni DHBT electrode in a 0.001 M K_2IrCl_6 + 0.01 M HCl solution for different periods. The mechanisms responsible for the spontaneous deposition of Ir on Ni substrate were previously studied [25,35]. In an acidic electrolyte, the dissolution of metallic Ni occurs according to equation 2 and 3. Metallic Ir deposition occurs according to equation 3.

$$2H^+ + Ni \rightleftarrows H_2 + Ni^{2+} \qquad \textit{Equation 2}$$

$$[IrCl_6]^{2-} + 2Ni \rightleftarrows Ir + 2Ni^{2+} + 6Cl^- \qquad \textit{Equation 3}$$

The concentration of Ni and Ir in solution was measured as a function of the immersion time (Figure 2) for Ni DHBT films immersed in 0.01 M HCl and in 0.001 M K_2IrCl_6 + 0.01 M HCl. In both cases, the Ni concentration increases linearly with immersion time, indicating that Ni is dissolved. In HCl only, equation 2 governs the reaction, and the dissolution rate of Ni is 3.80 ppm h^{-1} cm^{-2} (6.5×10^{-8} mol ml^{-1} h^{-1} cm^{-2}). In the presence of K_2IrCl_6, reaction 3 also occurs, and the dissolution rate of Ni increases to 4.49 ppm h^{-1} cm^{-2} (7.7×10^{-8} mol ml^{-1} h^{-1} cm^{-2}). In that later case, the Ir^{+4} concentration in the electrolyte decreases slowly, at a rate of 1.6 ppm h^{-1} cm^{-2} (0.8×10^{-8} mol ml^{-1} h^{-1} cm^{-2}). Based on the measured concentration of Ir^{+4} in solution, one would expect the Ni dissolution rate to reach 1.6×10^{-8} mol ml^{-1} h^{-1} cm^{-2} if both reactions 2 and 3 were occurring simultaneously. Instead, the dissolution rate of Ni is only increased by

1.2×10^{-8} mol ml^{-1} h^{-1} cm^{-2}. This suggests that reactions 2 and 3 are not occurring simultaneously, most probably because they are competing for the same Ni sites at the electrode surface.

High-resolution SEM was used to probe the internal structure of Ni DHBT deposit. It is seen that they are made of granular Ni covered by flake-like nanosheets (Figure 3a). Ir decoration of Ni DHBT films (Ir/Ni DHBT) was performed by immersing freshly prepared Ni/DHBT electrodes in a 0.001 M K_2IrCl_6 + 0.01 M HCl precursor solution. The morphology of an Ir/Ni DHBT film after 17 h of immersion is shown in Figures 1b and 3b. No significant change in the morphology of the films was observed compared to pristine Ni DHBT films. For comparison, a freshly prepared Ni DHBT film was immersed for 17h in a 0.01 M HCl solution (without K_2IrCl_6), hereafter denoted as eroded Ni DHBT. Again, no significant change of morphology was seen (Figure 3c). The Ir / Ir + Ni atomic ratio after 17 h of immersion, as determined from EDX analysis, was 0.3 %.

XPS measurements were conducted right after Ni DHBT and Ir/Ni DHBT coatings were prepared. Figure 4a shows the Ni 2p core levels of both electrodes. For as-prepared Ni DHBT, peaks are observed at 852.8eV and 870.1eV that are assigned to metallic Ni $2p_{3/2}$ and Ni $2p_{1/2}$ core levels, respectively [36]. Ni $2p_{3/2}$ and Ni $2p_{1/2}$ core level peaks are seen also at 856.4 and 874.1 eV, which are assigned to Ni hydroxide or Ni oxyhydroxide. The 3p core level peaks of metallic Ni and Ni hydroxide or Ni oxyhydroxide are observed at 66.3 and 68.0 eV, respectively [37]. In the case of Ir/Ni DHBT (Figure 4b), Ir $4f_{7/2}$ and Ir $4f_{5/2}$ core level peaks are observed at 60.4 and 63.5 eV, respectively. They are assigned to metallic iridium [38], which is consistent with Equation 3 describing the mechanisms underlying the galvanic reaction. Following immersion in the Ir-containing solution, there is almost no metallic Ni left at the surface. From the XPS data, the Ir / Ir + Ni surface atomic ratio is 5.3 %, much larger than the one determined from EDX measurements, which are more bulk sensitive. This reflects the fact that Ir atoms are located at the electrode surface.

The X-ray diffraction of Ni and Ir/Ni DHBT film were identical (Figure S1). This suggests that the bulk of both Ni DHBT and Ir/Ni DHBT films is composed only of polycrystalline Ni, and that metallic Ir decoration is occurring only at the surface. Most probably, the amount of Ir atoms at the electrode surface is too small to be detected by XRD performed in the Bragg-Brentano geometry.

Electrochemical characterization

Steady-state CVs of Ni, Ir/Ni DHBT and eroded Ni DHBT films recorded in 1M KOH at 5 mV s^{-1} are shown in Figure 5a. On Ni DHBT, the redox peaks associated with the reversible Ni/α-$Ni(OH)_2$ transition expected between -0.1V *vs* RHE and 0.3 V *vs* RHE were not observed [39,40]. This was expected since these CVs were recorded after a series of CVs performed between −0.10 to 1.5 V *vs* RHE, in a potential region where α-$Ni(OH)_2$ was irreversibly converted to β-$Ni(OH)_2$. In contrast, the CVs of Ir/Ni DHBT exhibited a pair of oxidation and reduction peaks in the 0.05 to 0.3 V *vs* RHE region (Figure 5a). They were associated with the underpotential deposition/stripping of hydrogen, H_{upd}, on metallic Ir [41,42]. Also, two broad oxidation/reduction peaks were observed at *ca.* 0.64 V *vs* RHE/0.53 V *vs* RHE, which are attributed to the reversible Ir (III)/Ir(IV) redox transition [18,19]. From 1.1 to 1.4 V *vs* RHE (Figure 5a), the oxidation and reduction peaks associated with the $Ni(OH)_2$/β-NiOOH redox couple were observed at 1.38 V and 1.26 V, respectively [26]. The background current density between 0.4 and 1.1 V was larger on Ir/Ni DHBT compared to Ni DHBT. This is consistent with the conversion of Ir to iridium oxy-hydroxide in this potential region [18]. All this evidence points to the fact that both Ni and Ir are present on the electrode surface and can participate in various redox reactions.

In the CVs of Figure 5b, there was a steep increase of current at potentials more positive than 1.6 V for Ni DHBT and eroded Ni DHBT, and at potentials greater than 1.43 V for Ir/Ni DHBT. This current increase was associated with oxygen evolution. Clearly, Ir/Ni DHBT was the most active electrode for the OER. It is worth noting that erosion of Ni DHBT through soaking in HCl had only a marginal effect on the OER characteristic compared to pristine Ni DHBT. Clearly, the presence of Ir sites on the surface of Ni is the key to increasing the OER performance of the DHBT electrode.

Steady-state CVs of Ir/Ni DHBT electrode after different immersion times were recorded (Figure S2). The relative amount of Ni atoms was evaluated by integration of the charge, Q_c, under the cathodic peak at *ca.* 1.20 V. Q_c increases steadily with the immersion time, from 0.22 C cm^{-2} to 2.11 C cm^{-2} after 20 h of immersion in a solution containing Ir^{+4} (Figure 5b). This is a factor of ten difference. In contrast, Q_c of eroded Ni DHBT is only 0.368 C cm^{-2} after 17 h of immersion, only a factor of 1.7 larger than pristine Ni DHBT. Therefore, even if the dissolution rate of Ni is only marginally increased from 3.80 to 4.49 ppm h^{-1} cm^{-2}, the presence of Ir^{+4} in solution greatly increased the number of Ni atoms able to participate in the $Ni(OH)_2$/β-NiOOH redox reaction. One possible explanation for the significant increase of Q_c is that Ir deposited through the galvanic replacement reaction had permanently altered the porous structure of the film and/or its wettability, the electrolyte having more readily access to a larger fraction of the Ni porous structure after immersion in the Ir^{+4} containing solution. This hypothesis will receive further traction in the next section.

Following immersion, Ir atoms at the electrode surface are mostly in a metallic state Similar to Pt, hydrogen atom can be underpotentially deposited and stripped from Ir metal [41,42]. The relative amount of Ir atoms able to participate in an electrochemical reaction was evaluated from the integration of the stripping peak of hydrogen underpotentially deposited on Ir, $Q_{H\ UPD}$. The CVs used to evaluate $Q_{H\ UPD}$ were obtained on as-immersed electrodes, before they were polarized in the potential region where the OER occurs. These results are shown in Figure S3a, and the method used to calculate $Q_{H\ UPD}$ is illustrated in Figure S3b. The variation of $Q_{H\ UPD}$, and the corresponding Ir surface concentration, are shown in Figure 5c and 5d, respectively. There is a linear relationship between the concentration of Ir atoms at the electrode surface and the immersion time. From these data, we can infer that Ir atoms exist at the surface of the Ir/Ni DHBT electrode as 4.3 nm clusters and there are 4.7×10^{15} clusters for an electrode geometrical surface area of 1 cm^2 (see the supplementary section for the detailed calculation).

Transmission electron microscopy (TEM) was used to determine the size and morphology of the iridium structures present on the surface of the 17h immersed Ir/Ni DHBT electrode. Figure 6a shows a TEM micrograph alongside HAADF-STEM (Figure 6b) and EDS mapping (Figure 6c-e) measurements. On the surface of the particle collected from the Ni DHBT film, small iridium clusters with a diameter in the range of 3-5 nm were observed, consistent with the size that was inferred from electrochemical measurements. Additionally, the presence of iridium was observed throughout the entire catalyst particle, potentially in the form of small clusters or single atoms.

OER performance

The activity for the OER of Ni and Ir/Ni DHBT films was investigated through chronopotentiometry measurements at 10 mA cm^{-2} (Figure 7a). In the case of Ni DHBT and Ir/Ni DHBT after 17h of immersion, the *iR*-corrected overpotentials to achieve 10 mA cm^{-2}, η_{10}, were 323 mV and 195 mV, respectively. The effect of the immersion time, and thus of the amount of Ir atoms, on η_{10} is depicted in Figure 7b. The overpotential decreased exponentially with increasing immersion time, with an exponential decay constant of 1.9 h. The η_{10} value reached a plateau after about 10h of immersion. In comparison, η_{10} of eroded Ni DHBT (17 h) was 327 mV, almost identical to pristine Ni DHBT. The increased activity of Ir/Ni DHBT compared to both Ni DHBT and eroded Ni DHBT could be due to the observed increase of electrochemically active surface area, as assessed by Q_c, and the presence of Ir atoms at the electrode surface. The relative importance of these two factors will be established later.

Figure 7c shows Tafel plots of Ni DHBT, eroded Ni DHBT and 17h-immersed Ir/Ni DHBT films. Tafel plots of replicates of the best performing electrodes are shown in Figure S4. The Tafel plot of eroded Ni DHBT is almost superimposable on Ni DHBT. Ni DHBT exhibited a Tafel slope of 52 mV dec^{-1} and an exchange current density of 7.9×10^{-6} mA cm^{-2}. Ir/Ni DHBT had a similar Tafel slope (49 mV dec^{-1}) but a much larger exchange current density of 7.9×10^{-4} mA cm^{-2}. This is a factor of 100 times larger than on Ni DHBT. The similarity between the Tafel slopes suggests that the rate-determining step for the OER on Ni DHBT and Ir/Ni DHBT is the same, and that the OER is proceeding with the same mechanism on both electrodes [44].

It is known in the literature that minute amounts of iron atoms at the electrode surface can dramatically increase the electrocatalytic activity of nickel for the OER elements [6,7]. In Figure S5, we are comparing the Tafel plots of Ni DHBT in 1M KOH, Ni DHBT in M KOH + 10 ppm of Fe ($FeCl_2\cdot6H_2O$), Ir/NiDHBT in 1M KOH, and Ir/Ni DHBT in 1M KOH + 10 ppm of Fe ($FeCl_2\cdot6H_2O$). Not surprisingly, the OER activity of the Ni DHBT electrode is increased by the addition of 10 ppm of Fe to the electrolyte.

However, this increase of activity is still much less than observed on the Ir/Ni DHBT electrode when tested in 1M KOH. In that later case, adding 10 ppm of Fe to the electrolyte only marginally increase the OER performances. Clearly, there is a real advantage in depositing minute amount of Ir atoms through the galvanic replacement reaction on Ni DHBT electrodes.

XPS characterization after electrochemistry

The surface electronic structure of Ni and Ir/Ni DHBT electrodes following the OER was investigated by X-ray photoelectron spectroscopy. Figure 8a and 8b show the Ir 4f core level peaks of Ir/Ni DHBT electrode before (as-deposited) and after electrochemical characterization in the OER region. After electrochemistry, the metallic Ir peaks at 60.4 and 63.5 eV are barely discernible, and two additional peaks were observed at 62.9 and 65.6 eV that corresponds to the Ir $4f_{7/2}$ and Ir $4f_{5/2}$ core level peaks of iridium oxide [45]. This is consistent with the literature, showing that a monolayer of iridium oxide was starting to form at potential more positive than *ca.* 0.6V *vs* RHE [19], and that a thick oxide layer was growing at potentials larger than 1.3V *vs* RHE [46].

The Ni $2p_{3/2}$ core level peaks of Ni and Ir/Ni DHBT electrodes after electrochemistry are shown in Figure 8c and 8d, respectively. As expected from the fact that large positive potentials were applied, both samples show typical line shapes of oxidized Ni, with only very small features at 852.8eV and 870.1eV assigned to metallic Ni $2p_{3/2}$ and Ni $2p_{1/2}$ core levels, respectively.

Fitting of the Ni $2p_{3/2}$ peaks was achieved using two components at 855.4 eV and 856.9 eV (Figure S6), which according to Ratcliff *et al.* are assigned to Ni^{2+} and Ni^{3+}, respectively [36]. There was no evidence of a peak at 854.0 eV that could be assigned to NiO [47]. Following the OER, the Ni^{3+}/Ni^{2+} ratio of the Ir/Ni DHBT film is 0.58:1, greater than the Ni^{3+}/Ni^{2+} ratio of as deposited Ni DHBT film, which is 0.23:1. The Ni^{3+} state is usually ascribed to the creation of vacancies in $Ni(OH)_2$ or to the presence of NiOOH[46–50] and is responsible for an increase of the electrode wettability [51,52]. Based on this evidence, one could argue that the increased hydrophilic character of Ir/Ni DHBT compared to Ni DHBT have an influence on the electrocatalytic properties of this electrode, especially on the way oxygen bubbles formed and detached from the electrode. This is going to be investigated through *in operando* acoustic emission.

Operando AE detection of bubbles during the OER

In a porous media, the following equation is valid[53]

$$P_g - P_w = P_c = -\frac{2\gamma\cos\theta}{r_c} \qquad \textit{Equation 4}$$

where P_g is the gas pressure (in Pa), P_w is the water pressure (in Pa), P_c is the capillary pressure (in Pa), γ is the surface tension of the electrolyte (in N m^{-1}), θ is the contact angle that the electrolyte would make with a flat surface of identical nature and structure (in radians or degrees), and r_c is the radius of the pore throat (in m). Increasing the hydrophilicity of the material through an increase in the Ni^{+3}/Ni^{+2} ratio would decrease the contact angle, which means that both P_g and P_c would be decreased. For a bubble to escape from the porous structure of an electrode P_g should be larger than P_c. Accordingly, if the value of P_g of Ir/Ni DHBT is smaller than P_g of Ni DHBT, this translates into smaller bubble size for the former electrode compared to the latter.

The verification of that hypothesis demands an investigation of the trapped gas in the porous DHBT electrodes. However, applying visualization technologies, like high-speed camera or computed tomography, to directly observed trapped gas bubbles in porous films is challenging[31,54–59]. In contrast, acoustic emission (AE) detection is a robust and straightforward method to perform *in operando* investigation of the behavior of gas bubbles at gas evolving electrode. With an AE sensor in close proximity to the working electrode, the acoustic signal generated by vibrating gas bubbles can be recorded. Then, the AE signal can be used to count the number of gas bubbles. Also, based on the work of Vazquez *et al.*[60], the bubble size can be determined using the Minnaert equation (Equation 5), which relates the AE frequency to the diameter of a bubble.

$$f_0 = \frac{1}{\pi D}\sqrt{\frac{3\gamma P^0}{\rho}} \qquad \textit{Equation 5}$$

where f_0 is the frequency of a bubble (in Hz), D is the bubble diameter (in m), and γ is the polytropic coefficient (without unit), P^0 is the ambient pressure (in Pa) and ρ is the density of water (in kg m^{-3}).

Figure 9a and 9b show the schematic of the acoustic detection system in combination with a three-electrode electrochemical cell setup. With this setup, the AE events during the OER were detected. With Ni and Ir/Ni DHBT electrodes, the AE events happened only upon the application of an anodic current (Figure S7). The AE signal was measured at 6.6 mA cm^{-2} for 300s. The peak frequencies of all AE events were translated into bubble size using the Minnaert equation (Equation 5). The distributions of bubble sizes are shown in Figure 9c, and the moving average of bubble size with respect to electrolysis time are shown in Figure 9d. For Ni DHBT, there are two main populations of bubbles, centered at 137 and 157 μm in diameter. For Ir/Ni DHBT, bubbles with 137 and 157 μm diameters are present, but there were a larger number of bubbles with diameters between 80 and 130 μm. The mean bubble diameter on Ni DHBT is 140 μm compared to 125 μm for Ir/Ni DHBT (Figure 9d). As shown in Figure S8 and S9, the mean bubble diameter of both Ni and Ir/Ni DHBT is independent of the current density between 1 and 6.6 mA cm^{-2}. Measurements at larger current density could not be performed since the AE detector was saturated. On Ir/Ni DHBT, there is a sizeable reduction of the bubble size compared to Ni DHBT, which is ascribed to the increased hydrophilicity of the former electrode compared to the latter.

EIS characterization

EIS measurements were conducted at different potentials for Ni DHBT and 17h immersed Ir/Ni DHBT films (Figure 10). The EIS spectra of both electrodes display a straight line in the high frequency region and one depressed semicircle in the low frequency region. The shape of the high frequency line does not change with the electrode potential. This is an indication that the features in the high-frequency response were not related to the OER kinetics. It is known that features in the high frequency region of EIS spectra are related to the electrode porosity[61,62]. The inclination of this line with respect to the horizontal-axis was 45° and 22.5° for Ni and 17 h immersed Ir/Ni DHBT electrode, respectively, indicating that the porous structures of these electrodes differ greatly. Eroded Ni DHBT electrodes share the same 45° line as observed for Ni DHBT (Figure S10), indicating that exposure to HCl only was not enough to modify the porous structure of the electrode.

The EIS data were fitted using a transmission line model and the de Levie equation 1, which assumes that pores are parallel with a cross-sectional shape independent of depth. The de Levie equation yielded a good fit for the 45° line observed for Ni DHBT and eroded Ni DHBT, indicating that the pores of these two electrodes are parallel with a cross-sectional shape independent of depth. In contrast, it failed to account for the 22.5° line observed in the high frequency region of Ir/Ni DHBT, suggesting that the pore structure was modified during the galvanic replacement reaction, and that a more detailed model to account for the porosity of Ir/Ni DHBT electrode needs to be developed.

The de Levie equation assumed that simple parallel pores are present. This is shown schematically in Figure 11a, where only the primary pore structure exists. However, the actual pore geometry could be branch-like as illustrated in Figure 11b, with a secondary pore structure that exists but remains inert (inactive) on Ni DHBT and eroded Ni DHBT coatings. In that case, the simple pore model would still be adequate to explain the EIS results. Alternatively, the actual pore geometry could be branch-like as illustrated in Figure 11c, with a secondary pore structure that is present and active, contributing to the EIS response. Accounting for the primary and secondary pore structure depicted in Figure 11c was achieved using the branched pore model developed by Itagaki [61]

$$Z = R_s + \frac{1}{\frac{1}{Z_{flat}} + \frac{n_{pore,1}}{Z_{pore,1}}} \qquad \textit{Equation 6}$$

$$z_{pore,1} = \sqrt{R_{\Omega,pore1} z_1^*} coth \sqrt{\frac{R_{\Omega,pore1}}{z_1^*}} X_1 \qquad \textit{Equation 7}$$

$$z_1^* = \left[\frac{1}{\left(\frac{1}{z_{pore,2}/(n_{pore,2}\xi)} + (1-\xi)(\frac{1}{R_{ct}^*} + i\omega C_{dl}^*) \right)} \right] \frac{1}{2\pi r_1} \qquad \textit{Equation 8}$$

$$z_{pore,2} = \sqrt{R_{\Omega,pore2} z_2^*} coth \sqrt{\frac{R_{\Omega,pore2}}{z_2^*}} X_2 \qquad \textit{Equation 9}$$

$$z_2^* = \left(\frac{1}{\frac{1}{R_{ct}^*} + i\omega C_{dl}^*} \right) \frac{1}{2\pi r_2} \qquad \textit{Equation 10}$$

where the z_{flat} is the impedance of the flat part outside the orifice of pores, z_1* and z_2* are the electrode interfacial impedance per unit length in the primary pore and secondary pore, respectively; $z_{pore,1}$ and $z_{pore,2}$ are the impedance of primary and secondary pores, respectively; $R_{\Omega,pore1}$ and $R_{\Omega,pore2}$ are the solution resistance per unit length in the primary pore and secondary pore, respectively; r_1 and r_2 represent the primary pore and secondary pore, respectively; X_1 and X_2 represent the length of the primary pore and secondary pore, respectively; ξ is the area fraction of secondary pore on the primary pore wall; $n_{pore,1}$ is the number of primary pores; $n_{pore,2}$ is the number of secondary pore per unit area of primary pore wall; $R_{ct}*$ is the specific charge transfer resistance in Ω cm^2; and $C_{dl}*$ represents the intrinsic double layer capacitance per unit area.

Figure 12 shows a simulation of the EIS data of Ni DHBT where only the primary pores were considered ($\xi = 0$). All the parameters were optimized using CNLS fittings, and the fitting parameters are presented in Table S1. The diameter and length of the primary pores were fixed at 22 μm and 95 μm to be consistent with the SEM micrographs. As shown in Figure 12, the agreement between the fitted and the experimental data of Ni DHBT is excellent, and the 45° line at high frequency is well accounted for. This is not surprising considering that the expression for the pore impedance (Equation 6) is identical to the de Levie equation when $\xi = 0$, and that the de Levie equation was giving a good fit of the high frequency region for Ni DHBT. The same set of equations can be used to account for both primary and secondary pores by having $\xi \neq 0$. As seen in Figure S11, $\xi = 0.3$ gives the best fit to the high frequency EIS data of Ir/Ni DHBT. Therefore, it was hypothesized that the secondary pores occupied 30% of the primary pore wall area, that the diameter of the secondary pores was 30% of the primary pore diameter, and that the length of the secondary pores was 30% of the primary pore length. This is consistent with the fact that the Ni DHBT electrode has a fractal surface[26]. Using the parameters given in Table S1, a good agreement was found between the fitted and the experimental data of Ir/Ni DHBT (Figure 12). More specifically, this model succeeded in yielding a straight line in the high frequency region, with an inclination of 22.5°. For Ir/Ni DHBT, the EIS data in the high frequency region suggests that both the primary and the secondary pore structure is accessible, which is not the case for Ni DHBT and eroded Ni DHBT electrodes.

The double-layer capacitance, C_{dl}, and the total charge-transfer resistance, R_{ct}, of the electrodes were extracted from the parameters characterizing the depressed semicircle observed in the low frequency region, using the following equations

$$C_{dl} = c_{dl}/R_{\Omega} \qquad \textit{Equation 11}$$

$$R_{ct} = r_{ct}R_{\Omega} \qquad \textit{Equation 12}$$

Figure 13a and 13b show plots of $\log(1/R_{ct})$ *vs* potential of Ni and 17h immersed Ir/Ni DHBT electrodes. As expected, the slope of the current density (Tafel plot) and $\log(1/R_{ct})$ *vs* potential curves are the same.

Figure 13c shows the variation of C_{dl} as a function of potential of Ni DHBT, 17 h immersed Ir/Ni DHBT, and eroded Ni DHBT films. Again, comparing Ni DHBT and eroded Ni DHBT, there was almost no variation of the double layer capacitance following immersion in HCl only. In contrast, at the lowest electrode potential, there was almost a factor of 6 increase of C_{dl} following immersion in 0.01 M HCl and 0.001 M K_2IrCl_6. These results are consistent with the Q_c values found earlier through the integration of the charge under the cathodic peak associated with the reduction of $Ni(OH)_2$

EIS data were acquired from *ca.* 1.37 to 1.52 V. In this potential range, oxygen bubbles form and continuously detach from the electrode surface. It is therefore expected that the resistance of the solution will increase and thus the ohmic drop. This was observed in Figure 10c and 10d, as a gradual increase of the intercepts between the EIS data and the X-axis was observed as the electrode potential was increased. However, this effect was already taken into consideration since the *iR*-corrected electrode potentials were used to draw the Tafel plots. The presence of O_2 bubbles was also expected to decrease the electrochemical surface area (ECSA) by reducing the contact area between the electrode surface and the electrolyte. This effect was captured in Figure 13c, where the capacitance values of all electrodes decreased as the electrode potential is increased. The current density increases as the OER overpotential is increased, which translates into an increase of O_2 gas emitted by the electrode, thus decreasing the accessibility of the electrolyte to the electrode's active sites. Figure 13d and 13e show plots of the capacitance and the normalized capacitance with respect to the current density. While the capacitance of Ir/Ni DHBT decreases steadily with the current density, the capacitance of Ni DHBT and eroded Ni DHBT has decreased by 40% of their original values as the current density reaches 0.02 A cm^{-2}. In comparison, current density as large as 0.14 A cm^{-2} should be reached for the Ir/Ni DHBT electrode to lose 40% of its original capacitance value. It should be emphasized that this difference in behavior results from the galvanic replacement reaction as it is not observed on eroded Ni DHBT. This reflects the fact that the Ir/Ni DHBT electrode is more capable of releasing the oxygen gas produced during the OER, which is consistent with the fact that the size of the oxygen bubbles is reduced by almost 15% compared to the Ni DHBT electrode. Thus to summarize, the galvanic replacement reaction affects the structure and composition of the Ir/Ni DHBT electrode in three different ways: (i) Ir nanoclusters 3 -5 nm in diameter are deposited at the electrode surface, with potentially smaller Ir clusters or single Ir atoms; (ii) a secondary pore structure is created/revealed that increases the electrochemically active surface area by a factor of *ca.* 6; and (iii) the blocking effect of O_2 gas bubble is considerably reduced most probably due to a decrease of the O_2 bubble size.

The relative weight of these three factors can be assessed from the Tafel curves (Figure 7). At any given potential, there is a factor of 175 difference between the current density of Ni DHBT and Ir/Ni DHBT. This difference in activity is due to the presence of iridium, as immersing the Ni DHBT electrode in an acidic solution containing no Ir^{+4} cations result in only a marginal increase in the activity of the electrode. The galvanic replacement reaction increases the active electrochemical surface of the electrode by promoting the creation of a network of secondary pores, or by activating a network of secondary pores already present in the Ni DHBT electrode but inactive before the electrode was immersed in the solution containing Ir^{+4} cations. The other effect of iridium is to increase the hydrophilicity of the electrode, resulting in a decrease in the size of the oxygen bubbles and, as discussed above, a less drastic decrease of the active electrochemical surface area as the current for the OER increases. Therefore, to account for these two effects of iridium, the Tafel plots of Ni DHBT and Ir/Ni DHBT shown in Figure 7c, which are expressed with respect to the geometric surface area, were normalized by the capacitance values measured at each electrode potential, assuming a value of 470 μF cm^{-2} for the specific double layer capacitance[39]. Normalization by the capacitance measured in the potential range where the OER is taking place accounts for *(i)* the increase of the ECSA that occurs due to immersion of the electrode in a solution containing Ir^{+4} cations that was discussed in Figure 5c, and *(ii)* the decrease of the ECSA due to the presence of oxygen bubbles on the electrode surface that was discussed in Figure 13c and 13d. The ECSA-normalized Tafel plots of Ni DHBT and Ir/Ni DHBT electrodes are shown in Figure 7d. At any given potential, there is a factor of 33 difference between the ECSA-normalized current density of Ni/DHBT and Ir/Ni DHBT that should be attributed to the very presence of Ir clusters and maybe Ir single atoms at the electrode surface. This is not really surprising, as there are many works in the literature that have highlighted the beneficial effect of the presence of iridium on the electrocatalytic activity of Ni for the OER. However, what the present work clearly shows is that the effect of iridium deposited on a nickel electrode through a galvanic replacement reaction is not limited exclusively to a catalytic effect, as it would have been concluded in the absence of a detailed series of IES and AE measurements and analysis. The galvanic replacement reaction affects the ECSA of the electrode, optimizes its wettability and ability to make O_2 bubbles smaller, both of these effects have a non-negligible effect on increasing the OER performances of the resulting electrodes. In the future, it will be interesting to catalyze fractal nickel surfaces using the same galvanic replacement process but a different cation in order to separate the role of the process from that of the cation.

Conclusion

3D porous Ni DHBT films possess a fractal structure, providing a large electrochemical active surface area and super-aerophobic surface properties to the electrode, which are beneficial for the OER[26]. In this work, it was shown that the galvanic replacement reaction between Ni and Ir atoms leads to a drastic increase of the electrocatalytic properties of 3D porous Ni DHBT substrate for the OER. This can be explained not only by the fact that iridium is more active than nickel for the OER but also from the fact that the galvanic replacement reaction is leading to the creation/activation of a secondary pore structure that increases the electrochemically active surface area of the electrode by a factor of *ca*. 8-10. Moreover, the Ir/Ni DHBT electrode has superior hydrophilic properties that contribute also to the improvement of the electrocatalytic properties by reducing the O_2 bubble size, thereby causing a less drastic decrease of the

ECSA of the electrode as a result of the blocking effect of O_2 bubbles. The best electrode achieved an overpotential for the OER of only 195 mV at 10 mA cm^{-2}. This is remarkable considering the low Ir amount involved. This study provides a way to optimize the OER performance for nanostructured Ni-based electrodes.

Supporting Information

XRD patterns; Additional electrochemical measurements; Ir hydrogen underpotential deposition peak analysis; Notes for Ir cluster size estimation; Additional electrochemical characterization in electrolyte with spiked Fe; Additional information for Operando acoustic emission detection of bubbles during the OER; EIS plots of eroded Ni DHBT electrodes; Parameters for EIS simulations.

Acknowledgements

This research was conducted as part of the Engineered Nickel Catalysts for Electrochemical Clean Energy project administered from Queen’s University and supported by Grant No. RGPNM 477963-2015 under the Natural Sciences and Engineering Research Council of Canada (NSERC) Discovery Frontiers Program. Electron microscopy imaging and related characterization were conducted at the Canadian Centre for Electron Microscopy at McMaster University.

Reference

(1) Lewandowska-Bernat, A.; Desideri, U. Opportunities of Power-to-Gas Technology in Different Energy Systems Architectures. *Appl. Energy* **2018**, *228*, 57–67. https://doi.org/10.1016/j.apenergy.2018.06.001.

(2) Ping, Y.; Galli, G.; Goddard, W. A. Electronic Structure of IrO2: The Role of the Metal d Orbitals. *J. Phys. Chem. C* **2015**, *119* (21), 11570–11577. https://doi.org/10.1021/acs.jpcc.5b00861.

(3) Suen, N. T.; Hung, S. F.; Quan, Q.; Zhang, N.; Xu, Y. J.; Chen, H. M. Electrocatalysis for the Oxygen Evolution Reaction: Recent Development and Future Perspectives. *Chemical Society Reviews*. Royal Society of Chemistry January 21, 2017, pp 337–365. https://doi.org/10.1039/c6cs00328a.

(4) Li, Y.; Sun, Y.; Qin, Y.; Zhang, W.; Wang, L.; Luo, M.; Yang, H.; Guo, S. Recent Advances on Water-Splitting Electrocatalysis Mediated by Noble-Metal-Based Nanostructured Materials. *Advanced Energy Materials*. John Wiley & Sons, Ltd March 1, 2020, p 1903120. https://doi.org/10.1002/aenm.201903120.

(5) She, L.; Zhao, G.; Ma, T.; Chen, J.; Sun, W.; Pan, H. On the Durability of Iridium-Based Electrocatalysts toward the Oxygen Evolution Reaction under Acid Environment. *Adv. Funct. Mater.* **2022**, *32* (5), 2108465. https://doi.org/10.1002/ADFM.202108465.

(6) Trotochaud, L.; Young, S. L.; Ranney, J. K.; Boettcher, S. W. Nickel-Iron Oxyhydroxide Oxygen-Evolution Electrocatalysts: The Role of Intentional and Incidental Iron Incorporation. *J. Am. Chem. Soc.* **2014**, *136* (18), 6744–6753. https://doi.org/10.1021/ja502379c.

(7) Corrigan, D. A. The Catalysis of the Oxygen Evolution Reaction by Iron Impurities in Thin Film Nickel Oxide Electrodes. *J. Electrochem. Soc.* **1987**, *134* (2), 377–384. https://doi.org/10.1149/1.2100463.

(8) Vij, V.; Sultan, S.; Harzandi, A. M.; Meena, A.; Tiwari, J. N.; Lee, W. G.; Yoon, T.; Kim, K. S. Nickel-Based Electrocatalysts for Energy-Related Applications: Oxygen Reduction, Oxygen Evolution, and Hydrogen Evolution Reactions. *ACS Catal.* **2017**, *7* (10), 7196–7225. https://doi.org/10.1021/acscatal.7b01800.

(9) Shao, Q.; Wang, P.; Huang, X. Opportunities and Challenges of Interface Engineering in Bimetallic Nanostructure for Enhanced Electrocatalysis. *Adv. Funct. Mater.* **2019**, *29* (3), 1806419. https://doi.org/10.1002/adfm.201806419.

(10) Lim, J.; Yang, S.; Kim, C.; Roh, C. W.; Kwon, Y.; Kim, Y. T.; Lee, H. Shaped Ir–Ni Bimetallic Nanoparticles for Minimizing Ir Utilization in Oxygen Evolution Reaction. *Chem. Commun.* **2016**, *52* (32), 5641–5644. https://doi.org/10.1039/C6CC00053C.

(11) Pi, Y.; Shao, Q.; Wang, P.; Guo, J.; Huang, X.; Pi, Y.; Shao, Q.; Wang, P.; Huang, X.; Guo, J. General Formation of Monodisperse IrM (M = Ni, Co, Fe) Bimetallic Nanoclusters as Bifunctional Electrocatalysts for Acidic Overall Water Splitting. *Adv. Funct. Mater.* **2017**, *27* (27), 1700886. https://doi.org/10.1002/ADFM.201700886.

(12) Pi, Y.; Shao, Q.; Zhu, X.; Huang, X. Dynamic Structure Evolution of Composition Segregated Iridium-Nickel Rhombic Dodecahedra toward Efficient Oxygen Evolution Electrocatalysis. *ACS Nano* **2018**, *12* (7), 7371–7379. https://doi.org/10.1021/ACSNANO.8B04023/ASSET/IMAGES/LARGE/NN-2018-04023S_0006.JPEG.

(13) Wang, C.; Sui, Y.; Xu, M.; Liu, C.; Xiao, G.; Zou, B. Synthesis of Ni-Ir Nanocages with Improved Electrocatalytic Performance for the Oxygen Evolution Reaction. *ACS Sustain. Chem. Eng.* **2017**, *5* (11), 9787–9792. https://doi.org/10.1021/ACSSUSCHEMENG.7B01628/SUPPL_FILE/SC7B01628_SI_001.PDF.

(14) Nong, H. N.; Oh, H.-S.; Reier, T.; Willinger, E.; Willinger, M.-G.; Petkov, V.; Teschner, D.; Strasser, P.; Nong,] H N; Oh, H. S.; et al. Oxide-Supported IrNiOx Core–Shell Particles as Efficient, Cost-Effective, and Stable Catalysts for Electrochemical Water Splitting. *Angew. Chemie Int. Ed.* **2015**, *54* (10), 2975–2979. https://doi.org/10.1002/ANIE.201411072.

(15) Nong, H. N.; Reier, T.; Oh, H. S.; Gliech, M.; Paciok, P.; Vu, T. H. T.; Teschner, D.; Heggen, M.; Petkov, V.; Schlögl, R.; et al. A Unique Oxygen Ligand Environment Facilitates Water Oxidation in Hole-Doped IrNiOx Core–Shell

Electrocatalysts. *Nat. Catal. 2018 111* **2018**, *1* (11), 841–851. https://doi.org/10.1038/s41929-018-0153-y.

(16) Xu, S.; Chen, S.; Tian, L.; Xia, Q.; Hu, W. Selective-Leaching Method to Fabricate an Ir Surface-Enriched Ir-Ni Oxide Electrocatalyst for Water Oxidation. *J. Solid State Electrochem.* **2016**, *20* (7), 1961–1970. https://doi.org/10.1007/S10008-016-3200-0/FIGURES/8.

(17) Godínez-Salomón, F.; Albiter, L.; Alia, S. M.; Pivovar, B. S.; Camacho-Forero, L. E.; Balbuena, P. B.; Mendoza-Cruz, R.; Arellano-Jimenez, M. J.; Rhodes, C. P. Self-Supported Hydrous Iridium-Nickel Oxide Two-Dimensional Nanoframes for High Activity Oxygen Evolution Electrocatalysts. *ACS Catal.* **2018**, *8* (11), 10498–10520.

https://doi.org/10.1021/ACSCATAL.8B02171/SUPPL_FILE/CS8B02171_SI_001.PDF.

(18) Reier, T.; Pawolek, Z.; Cherevko, S.; Bruns, M.; Jones, T.; Teschner, D.; Selve, S.; Bergmann, A.; Nong, H. N.; Schlögl, R.; et al. Molecular Insight in Structure and Activity of Highly Efficient, Low-Ir Ir-Ni Oxide Catalysts for Electrochemical Water Splitting (OER). *J. Am. Chem. Soc.* **2015**, *137* (40), 13031–13040. https://doi.org/10.1021/jacs.5b07788.

(19) Papaderakis, A.; Pliatsikas, N.; Prochaska, C.; Vourlias, G.; Patsalas, P.; Tsiplakides, D.; Balomenou, S.; Sotiropoulos, S. Oxygen Evolution at IrO_2 Shell–Ir−Ni Core Electrodes Prepared by Galvanic Replacement. *J. Phys. Chem. C* **2016**, *120* (36), 19995–20005. https://doi.org/10.1021/ACS.JPCC.6B06025.

(20) Touni, A.; Papaderakis, A.; Karfaridis, D.; Vourlias, G.; Sotiropoulos, S. Oxygen Evolution Reaction at IrO2/Ir(Ni) Film Electrodes Prepared by Galvanic Replacement and Anodization: Effect of Precursor Ni Film Thickness. *Mol. 2019, Vol. 24, Page 2095* **2019**, *24* (11), 2095. https://doi.org/10.3390/MOLECULES24112095.

(21) Özer, E.; Sinev, I.; Mingers, A. M.; Araujo, J.; Kropp, T.; Mavrikakis, M.; Mayrhofer, K. J. J.; Cuenya, B. R.; Strasser, P. Ir-Ni Bimetallic OER Catalysts Prepared by Controlled Ni Electrodeposition on Irpoly and Ir(111). *Surfaces*

2018, Vol. 1, Pages 165-186 **2018**, *1* (1), 165–186. https://doi.org/10.3390/SURFACES1010013.

(22) Gong, L.; Ren, D.; Deng, Y.; Yeo, B. S. Efficient and Stable Evolution of Oxygen Using Pulse-Electrodeposited Ir/Ni Oxide Catalyst in Fe-Spiked KOH Electrolyte. *ACS Appl. Mater. Interfaces* **2016**, *8* (25), 15985–15990. https://doi.org/10.1021/ACSAMI.6B01888/SUPPL_FILE/AM6B01888_SI_001.PDF.

(23) Wang, Q.; Huang, X.; Zhao, Z. L.; Wang, M.; Xiang, B.; Li, J.; Feng, Z.; Xu, H.; Gu, M. Ultrahigh-Loading of Ir Single Atoms on NiO Matrix to Dramatically Enhance Oxygen Evolution Reaction. *J. Am. Chem. Soc.* **2020**, *142* (16), 7425–7433. https://doi.org/10.1021/JACS.9B12642/SUPPL_FILE/JA9B12642_SI_001.PDF.

(24) Wang, C.; Sui, Y.; Xu, M.; Liu, C.; Xiao, G.; Zou, B. Synthesis of Ni-Ir Nanocages with Improved Electrocatalytic Performance for the Oxygen Evolution Reaction. *ACS Sustain. Chem. Eng.* **2017**, *5* (11), 9787–9792. https://doi.org/10.1021/ACSSUSCHEMENG.7B01628/ASSET/IMAGES/LARGE/SC-2017-01628G_0006.JPEG.

(25) Mellsop, S. R.; Gardiner, A.; Marshall, A. T. Spontaneous Deposition of Iridium onto Nickel Substrates for the Oxygen Evolution Reaction. *Electrocatalysis* **2016**, *7* (3), 226–234. https://doi.org/10.1007/s12678-016-0299-9.

(26) Hao, M.; Charbonneau, V.; Fomena, N. N.; Gaudet, J.; Bruce, D. R.; Garbarino, S.; Harrington, D. A.; Guay, D. Hydrogen Bubble Templating of Fractal Ni Catalysts for Water Oxidation in Alkaline Media. *ACS Appl. Energy Mater.* **2019**, *2* (8), 5734–5743. https://doi.org/10.1021/acsaem.9b00860.

(27) Angulo, A.; van der Linde, P.; Gardeniers, H.; Modestino, M.; Fernández Rivas, D. Influence of Bubbles on the Energy Conversion Efficiency of Electrochemical Reactors. *Joule*. Cell Press March 18, 2020, pp 555–579. https://doi.org/10.1016/j.joule.2020.01.005.

(28) Yang, F.; Kim, M. J.; Brown, M.; Wiley, B. J. Alkaline Water Electrolysis at 25

A cm^{-2} with a Microfibrous Flow-through Electrode. *Adv. Energy Mater.* **2020**, *10* (25), 2001174. https://doi.org/10.1002/aenm.202001174.

(29) Kim, Y. J.; Lim, A.; Kim, J. M.; Lim, D.; Chae, K. H.; Cho, E. N.; Han, H. J.; Jeon, K. U.; Kim, M.; Lee, G. H.; et al. Highly Efficient Oxygen Evolution Reaction via Facile Bubble Transport Realized by Three-Dimensionally Stack-Printed Catalysts. *Nat. Commun.* **2020**, *11* (1), 1–11. https://doi.org/10.1038/s41467-020-18686-0.

(30) Li, Y.; Yang, G.; Yu, S.; Mo, J.; Li, K.; Xie, Z.; Ding, L.; Wang, W.; Zhang, F. Y. High-Speed Characterization of Two-Phase Flow and Bubble Dynamics in Titanium Felt Porous Media for Hydrogen Production. *Electrochim. Acta* **2021**, *370*, 137751. https://doi.org/10.1016/j.electacta.2021.137751.

(31) Iwata, R.; Zhang, L.; Wilke, K. L.; Gong, S.; He, M.; Gallant, B. M.; Wang, E. N. Bubble Growth and Departure Modes on Wettable/Non-Wettable Porous Foams in Alkaline Water Splitting. *Joule* **2021**, *5* (4), 887–900. https://doi.org/10.1016/j.joule.2021.02.015.

(32) Maier, M.; Meyer, Q.; Majasan, J.; Owen, R. E.; Robinson, J. B.; Dodwell, J.; Wu, Y.; Castanheira, L.; Hinds, G.; Shearing, P. R.; et al. Diagnosing Stagnant Gas Bubbles in a Polymer Electrolyte Membrane Water Electrolyser Using Acoustic Emission. *Front. Energy Res.* **2020**, *8*, 268. https://doi.org/10.3389/fenrg.2020.582919.

(33) Kou, T.; Wang, S.; Shi, R.; Zhang, T.; Chiovoloni, S.; Lu, J. Q.; Chen, W.; Worsley, M. A.; Wood, B. C.; Baker, S. E.; et al. Periodic Porous 3D Electrodes Mitigate Gas Bubble Traffic during Alkaline Water Electrolysis at High Current Densities. *Adv. Energy Mater.* **2020**, *10* (46), 2002955. https://doi.org/10.1002/aenm.202002955.

(34) de Levie, R. On the Impedance of Electrodes with Rough Interfaces. *J. Electroanal. Chem. Interfacial Electrochem.* **1989**, *261* (1), 1–9. https://doi.org/10.1016/0022-0728(89)87121-9.

(35) Duca, M.; Guerrini, E.; Colombo, A.; Trasatti, S. Activation of Nickel for Hydrogen Evolution by Spontaneous Deposition of Iridium. *Electrocatalysis*

2013, *4* (4), 338–345. https://doi.org/10.1007/s12678-013-0148-z.

(36) Ratcliff, E. L.; Meyer, J.; Steirer, K. X.; Garcia, A.; Berry, J. J.; Ginley, D. S.; Olson, D. C.; Kahn, A.; Armstrong, N. R. Evidence for Near-Surface NiOOH Species in Solution-Processed NiO x Selective Interlayer Materials: Impact on Energetics and the Performance of Polymer Bulk Heterojunction Photovoltaics. *Chem. Mater.* **2011**, *23* (22), 4988–5000. https://doi.org/10.1021/cm202296p.

(37) Bhattar, S.; Krishnakumar, A.; Kanitkar, S.; Abedin, A.; Shekhawat, D.; Haynes, D. J.; Spivey, J. J. 110th Anniversary: Dry Reforming of Methane over Ni-and Sr-Substituted Lanthanum Zirconate Pyrochlore Catalysts: Effect of Ni Loading. *Ind. Eng. Chem. Res.* **2019**, *58* (42), 19386–19396. https://doi.org/10.1021/acs.iecr.9b02434.

(38) Zhang, Y.; Wu, C.; Jiang, H.; Lin, Y.; Liu, H.; He, Q.; Chen, S.; Duan, T.; Song, L. Atomic Iridium Incorporated in Cobalt Hydroxide for Efficient Oxygen Evolution Catalysis in Neutral Electrolyte. *Adv. Mater.* **2018**, *30* (18), 1707522. https://doi.org/10.1002/adma.201707522.

(39) Hao, M.; Garbarino, S.; Prabhudev, S.; Borsboom-Hanson, T.; Botton, G. A.; Harrington, D. A.; Guay, D. Vertically Aligned Ni Nanowires as a Platform for Kinetically Limited Water-Splitting Electrocatalysis. *J. Phys. Chem. C* **2019**, *123* (2), 1082–1093. https://doi.org/10.1021/acs.jpcc.8b10414.

(40) Alsabet, M.; Grden, M.; Jerkiewicz, G. Electrochemical Growth of Surface Oxides on Nickel. Part 1: Formation of α-Ni(OH) 2 in Relation to the Polarization Potential, Polarization Time, and Temperature. *Electrocatalysis* **2011**, *2* (4), 317–330. https://doi.org/10.1007/s12678-011-0067-9.

(41) Gómez, R.; Weaver, M. J. Electrochemical Infrared Studies of Monocrystalline Iridium Surfaces. Part 2: Carbon Monoxide and Nitric Oxide Adsorption on Ir(110). *Langmuir* **1998**, *14* (9), 2525–2534. https://doi.org/10.1021/LA9711692.

(42) Woods, R. Hydrogen Adsorption on Platinum, Iridium and Rhodium Electrodes at Reduced Temperatures and the Determination of Real Surface Area. *J. Electroanal. Chem. Interfacial Electrochem.* **1974**, *49* (2), 217–226. https://doi.org/10.1016/S0022-0728(74)80229-9.

(43) Drault, F.; Comminges, C.; Can, F.; Pirault-Roy, L.; Epron, F.; Le Valant, A. Palladium, Iridium, and Rhodium Supported Catalysts: Predictive H2 Chemisorption by Statistical Cuboctahedron Clusters Model. *Mater. 2018, Vol. 11, Page 819* **2018**, *11* (5), 819. https://doi.org/10.3390/MA11050819.

(44) Fang, Y. H.; Liu, Z. P. Tafel Kinetics of Electrocatalytic Reactions: From Experiment to First-Principles. *ACS Catal.* **2014**, *4* (12), 4364–4376. https://doi.org/10.1021/CS501312V.

(45) Moulder, J. F.; Stickle, W. F.; Sobol, P. E.; Bomben, K. D. *Handbook of X-Ray Photoelectron Spectroscopy: A Reference Book of Standard Spectra for Identification and Interpretation of XPS Data*; Physical Electronics Inc.: Eden Prairie Minn., 1992.

(46) Mozota, J.; Conway, B. E. Surface and Bulk Processes at Oxidized Iridium Electrodes—I. Monolayer Stage and Transition to Reversible Multilayer Oxide Film Behaviour. *Electrochim. Acta* **1983**, *28* (1), 1–8. https://doi.org/10.1016/0013-4686(83)85079-8.

(47) Alsabet, M.; Grden, M.; Jerkiewicz, G. Electrochemical Growth of Surface Oxides on Nickel. Part 2: Formation of β-Ni(OH)2 and NiO in Relation to the Polarization Potential, Polarization Time, and Temperature. *Electrocatalysis* **2014**, *5* (2), 136–147. https://doi.org/10.1007/s12678-013-0172-z.

(48) Ratcliff, E. L.; Meyer, J.; Steirer, K. X.; Garcia, A.; Berry, J. J.; Ginley, D. S.; Olson, D. C.; Kahn, A.; Armstrong, N. R. Evidence for Near-Surface NiOOH Species in Solution-Processed NiO x Selective Interlayer Materials: Impact on Energetics and the Performance of Polymer Bulk Heterojunction Photovoltaics. *Chem. Mater.* **2011**, *23* (22), 4988–5000. https://doi.org/10.1021/cm202296p.

(49) Manders, J. R.; Tsang, S. W.; Hartel, M. J.; Lai, T. H.; Chen, S.; Amb, C. M.; Reynolds, J. R.; So, F. Solution-Processed Nickel Oxide Hole Transport Layers in High Efficiency Polymer Photovoltaic Cells. *Adv. Funct. Mater.* **2013**, *23* (23), 2993–3001. https://doi.org/10.1002/ADFM.201202269.

(50) Uhlenbrock, S.; Scharfschwerdt, C.; Neumann, M.; Illing, G.; Freund, H. J. The Influence of Defects on the Ni 2p and O 1s XPS of NiO. *J. Phys. Condens. Matter*

1992, *4* (40), 7973. https://doi.org/10.1088/0953-8984/4/40/009.

(51) Zhou, Q.; Chen, Y.; Zhao, G.; Lin, Y.; Yu, Z.; Xu, X.; Wang, X.; Liu, H. K.; Sun, W.; Dou, S. X. Active-Site-Enriched Iron-Doped Nickel/Cobalt Hydroxide Nanosheets for Enhanced Oxygen Evolution Reaction. *ACS Catal.* **2018**, *8* (6), 5382–5390. https://doi.org/10.1021/ACSCATAL.8B01332/SUPPL_FILE/CS8B01332_SI_001.PDF.

(52) Eslamibidgoli, M. J.; Groß, A.; Eikerling, M. Surface Configuration and Wettability of Nickel(Oxy)Hydroxides: A First-Principles Investigation. *Phys. Chem. Chem. Phys.* **2017**, *19* (34), 22659–22669. https://doi.org/10.1039/c7cp03396f.

(53) Tranter, T. G.; Boillat, P.; Mularczyk, A.; Manzi-Orezzoli, V.; Shearing, P. R.; Brett, D. J. L.; Eller, J.; Gostick, J. T.; Forner-Cuenca, A. Pore Network Modelling of Capillary Transport and Relative Diffusivity in Gas Diffusion Layers with Patterned Wettability. *J. Electrochem. Soc.* **2020**, *167* (11), 114512. https://doi.org/10.1149/1945-7111/ab9d61.

(54) Kou, T.; Wang, S.; Shi, R.; Zhang, T.; Chiovoloni, S.; Lu, J. Q.; Chen, W.; Worsley, M. A.; Wood, B. C.; Baker, S. E.; et al. Periodic Porous 3D Electrodes Mitigate Gas Bubble Traffic during Alkaline Water Electrolysis at High Current Densities. *Adv. Energy Mater.* **2020**, *10* (46), 2002955. https://doi.org/10.1002/aenm.202002955.

(55) Lee, J. K.; Lee, C. H.; Fahy, K. F.; Zhao, B.; LaManna, J. M.; Baltic, E.; Jacobson, D. L.; Hussey, D. S.; Bazylak, A. Critical Current Density as a Performance Indicator for Gas-Evolving Electrochemical Devices. *Cell Reports Phys. Sci.* **2020**, *1* (8), 100147. https://doi.org/10.1016/j.xcrp.2020.100147.

(56) Yang, F.; Kim, M. J.; Brown, M.; Wiley, B. J. Alkaline Water Electrolysis at 25 A Cm−2 with a Microfibrous Flow-through Electrode. *Adv. Energy Mater.* **2020**, *10* (25), 2001174. https://doi.org/10.1002/aenm.202001174.

(57) Kim, Y. J.; Lim, A.; Kim, J. M.; Lim, D.; Chae, K. H.; Cho, E. N.; Han, H. J.; Jeon, K. U.; Kim, M.; Lee, G. H.; et al. Highly Efficient Oxygen Evolution

Reaction via Facile Bubble Transport Realized by Three-Dimensionally Stack-Printed Catalysts. *Nat. Commun.* **2020**, *11* (1), 1–11. https://doi.org/10.1038/s41467-020-18686-0.

(58) Li, Y.; Yang, G.; Yu, S.; Mo, J.; Li, K.; Xie, Z.; Ding, L.; Wang, W.; Zhang, F.-Y. High-Speed Characterization of Two-Phase Flow and Bubble Dynamics in Titanium Felt Porous Media for Hydrogen Production. *Electrochim. Acta* **2021**, *370*, 137751. https://doi.org/10.1016/j.electacta.2021.137751.

(59) Li, K.; Wang, W.; Zheng, H.; Wang, X.; Xie, Z.; Ding, L.; Yu, S.; Yao, Y.; Zhang, F. Y. Visualizing Highly Selective Electrochemical CO2 Reduction on a Molecularly Dispersed Catalyst. *Mater. Today Phys.* **2021**, *19*, 100427. https://doi.org/10.1016/j.mtphys.2021.100427.

(60) Vazquez, A.; Manasseh, R.; Chicharro, R. Can Acoustic Emissions Be Used to Size Bubbles Seeping from a Sediment Bed? *Chem. Eng. Sci.* **2015**, *131*, 187–196. https://doi.org/10.1016/j.ces.2015.03.058.

(61) Itagaki, M.; Hatada, Y.; Shitanda, I.; Watanabe, K. Complex Impedance Spectra of Porous Electrode with Fractal Structure. *Electrochim. Acta* **2010**, *55* (21), 6255–6262. https://doi.org/10.1016/j.electacta.2009.10.016.

(62) Lasia, A. Electrochemical Impedance Spectroscopy and Its Applications. *Electrochem. Impedance Spectrosc. its Appl.* **2014**, *9781461489*, 1–367. https://doi.org/10.1007/978-1-4614-8933-7.

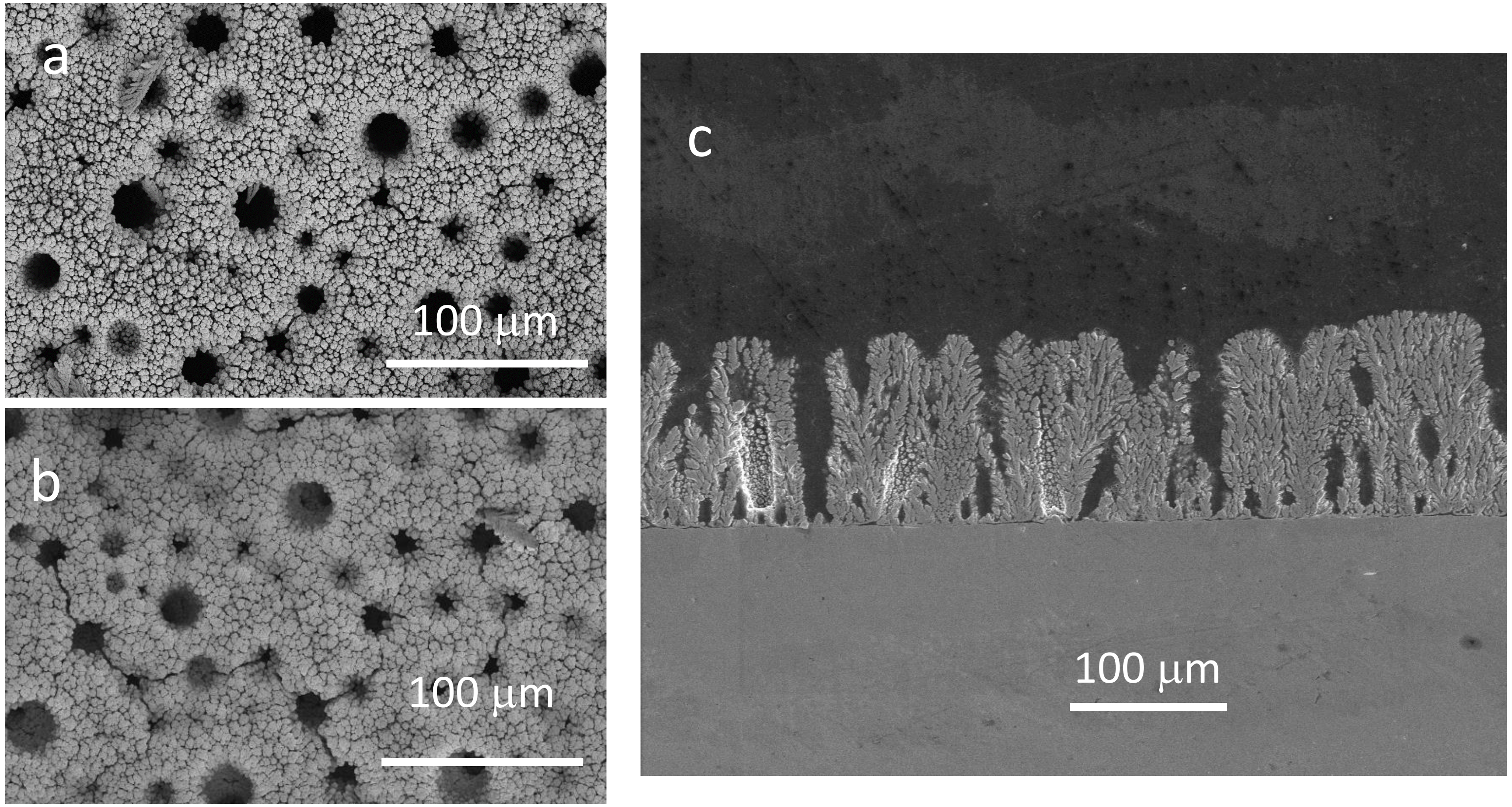

Figure 1 SEM image of a) Ni DHBT surface; b) Ir/Ni DHBT surface; c) of Ni DHBT cross-section.

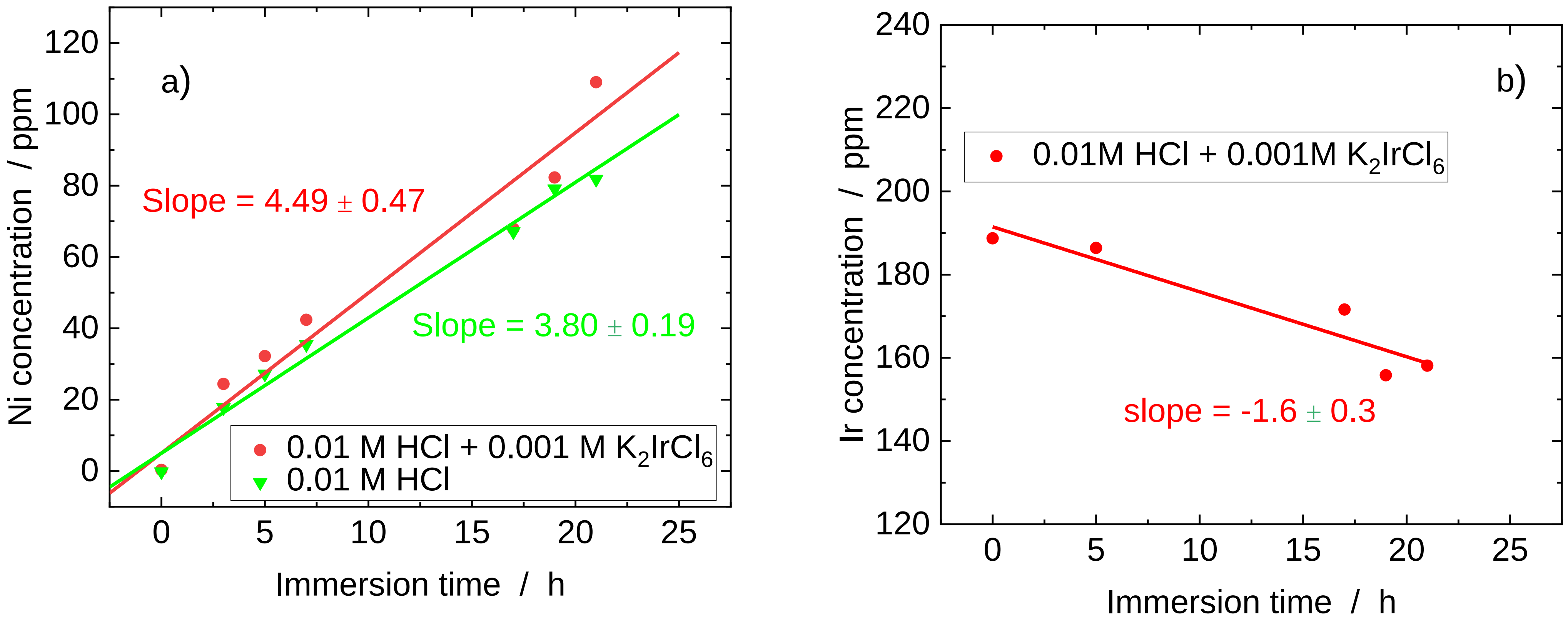

Figure 2 Variation of the concentrations of a) Ni and b) Ir in solution upon immersion of Ni DHBT films.

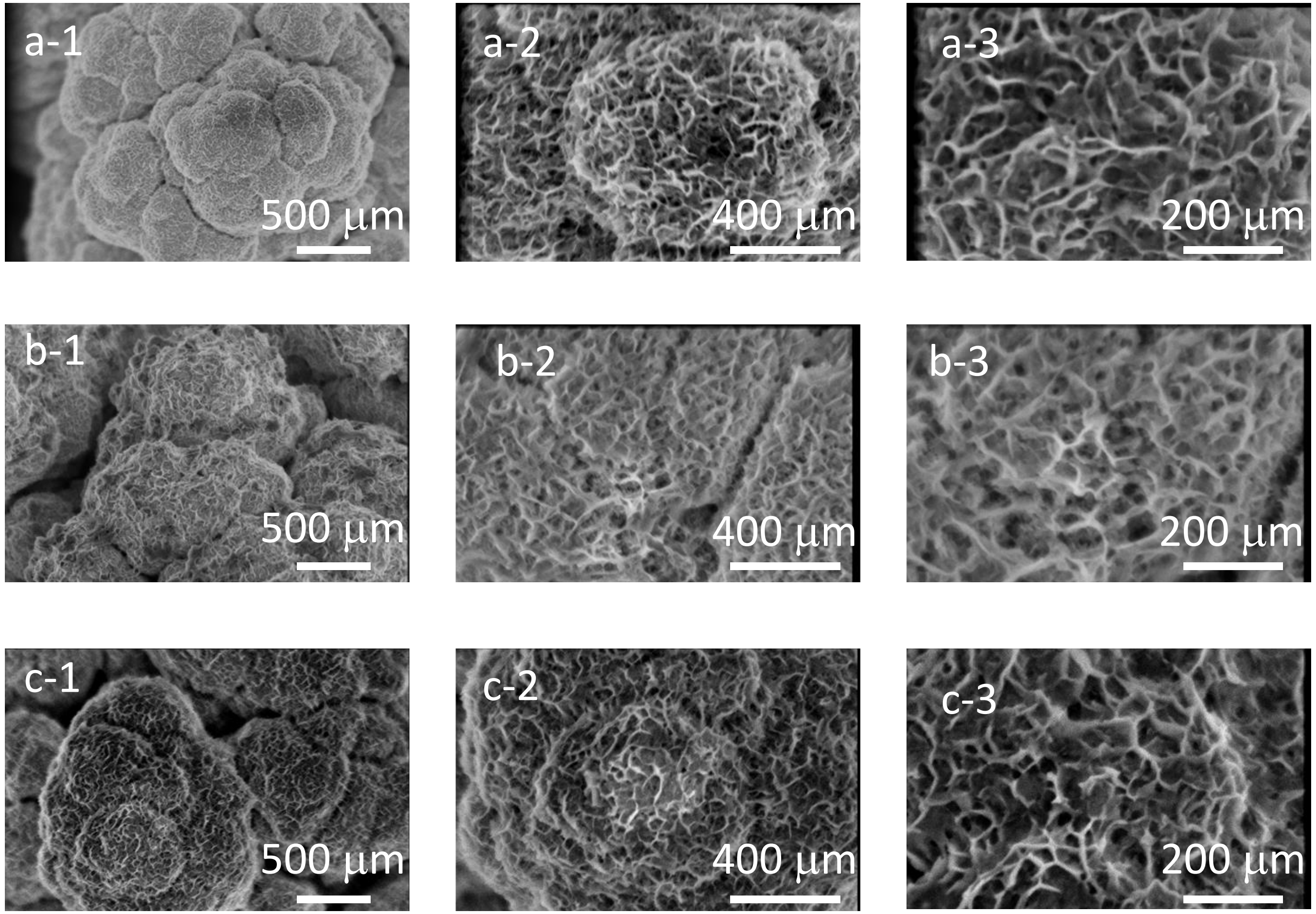

Figure 3 High resolution SEM images of a) Ni DHBT, b) Ir/Ni DHBT and c) corroded Ni DHBT at different magnifications.

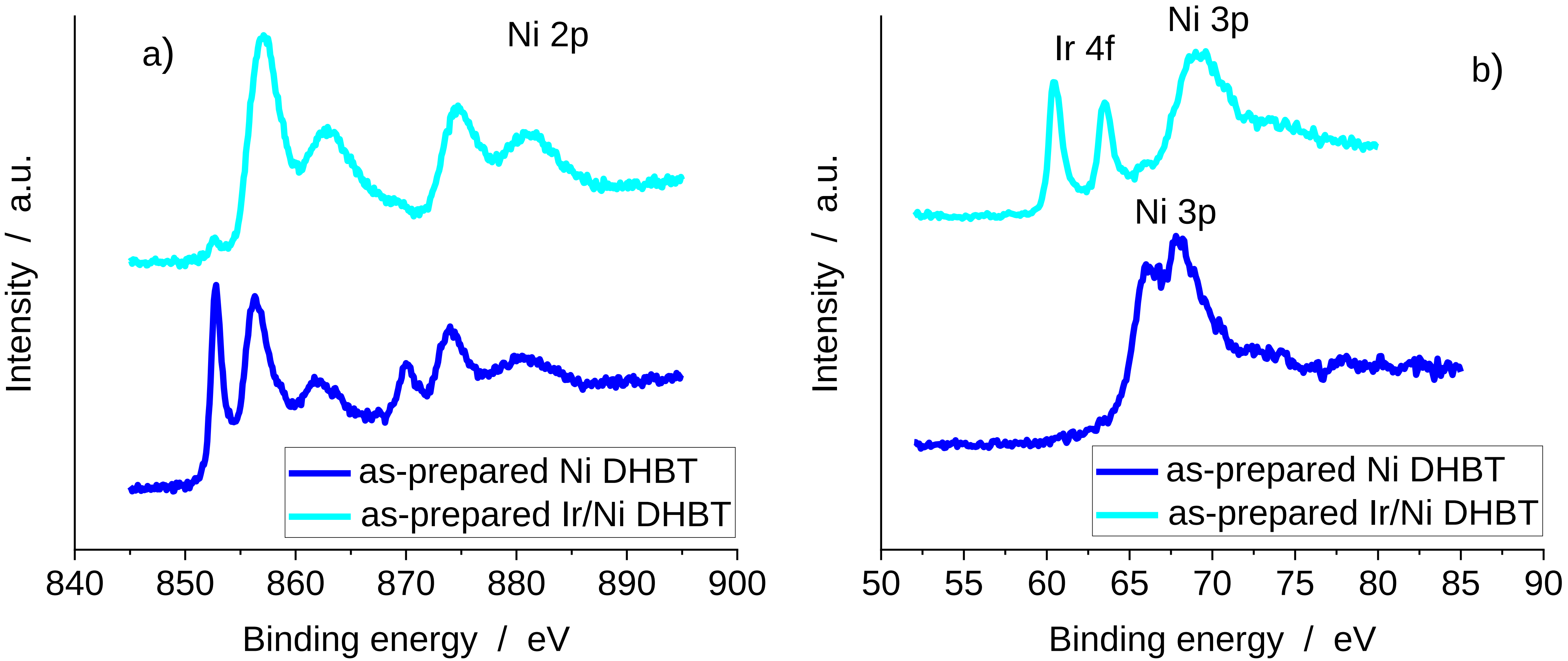

Figure 4 XPS for freshly prepared Ni DHBT film and Ir/Ni DHBT film: a) Ni 2p core level and b) Ir 4f and Ni 3p core levels.

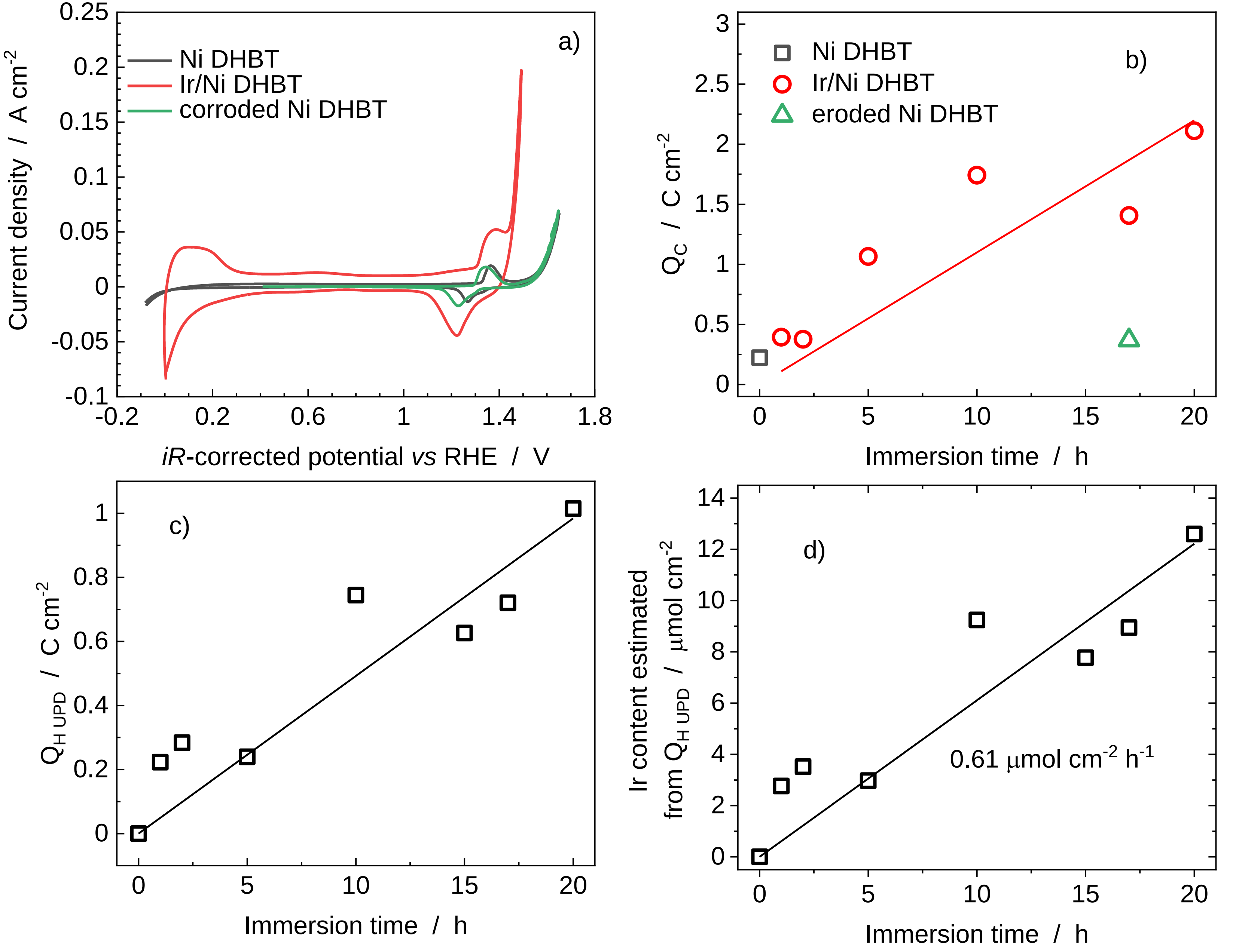

Figure 5 In a), CVs of Ni, Ir/Ni and eroded Ni DHBT films in 1 M KOH at 5 mV s^{-1}. In b), variation of the charge, Q_c, under the reduction peak of $Ni(OH)_2$ with the immersion time. In c), variation of the charge, Q_H UPD with the immersion time. In d), variation of the Ir content with the immersion time.

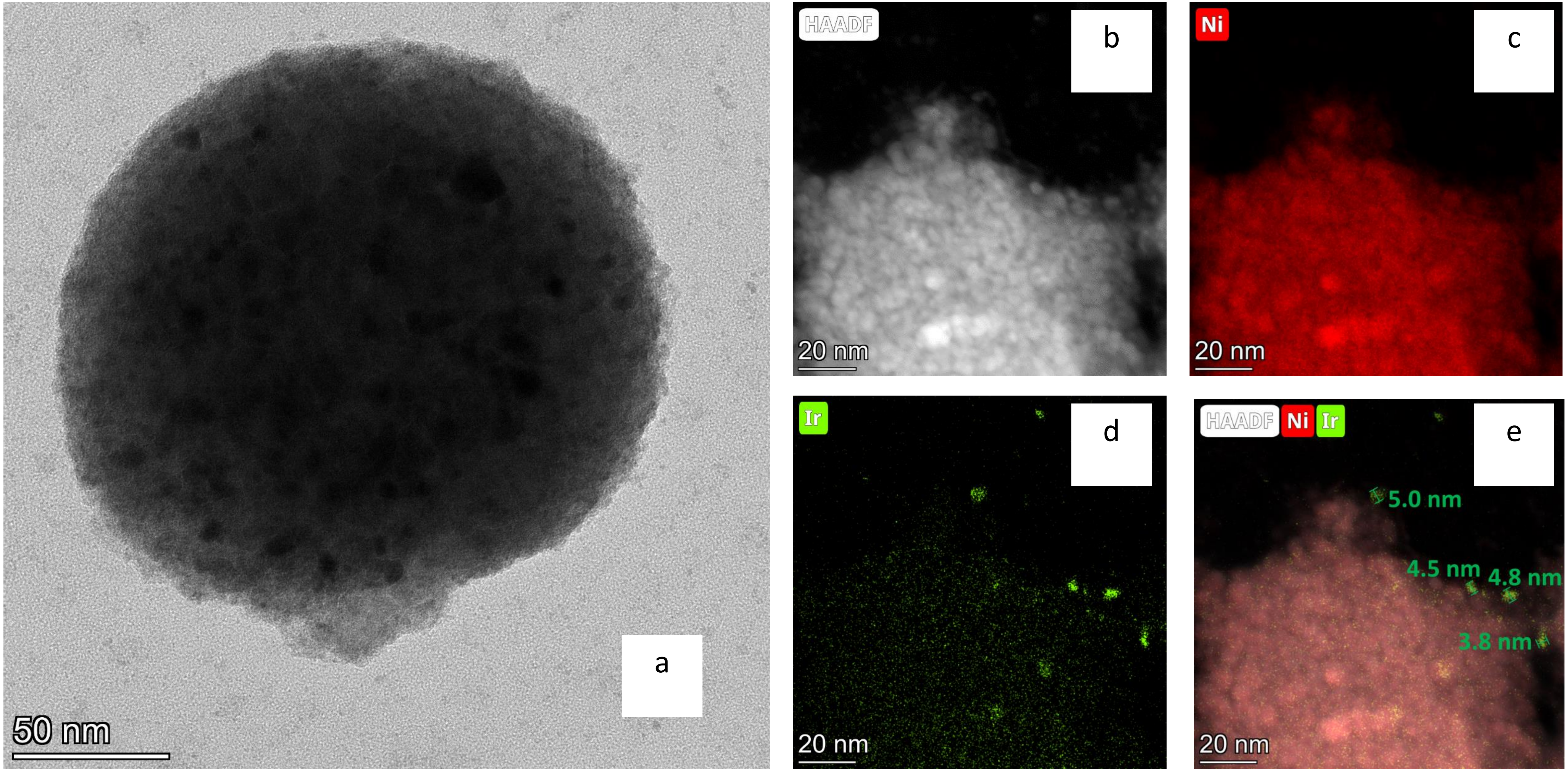

Figure 6 In a) TEM image of the 17h immersed Ir/Ni DHBT fragment. In b) HAADF-STEM images of the Ir/Ni DHBT fragment. In c) d) and e), EDS mappings showing the distribution of Ni and Ir on the Ir/Ni DHBT surface.

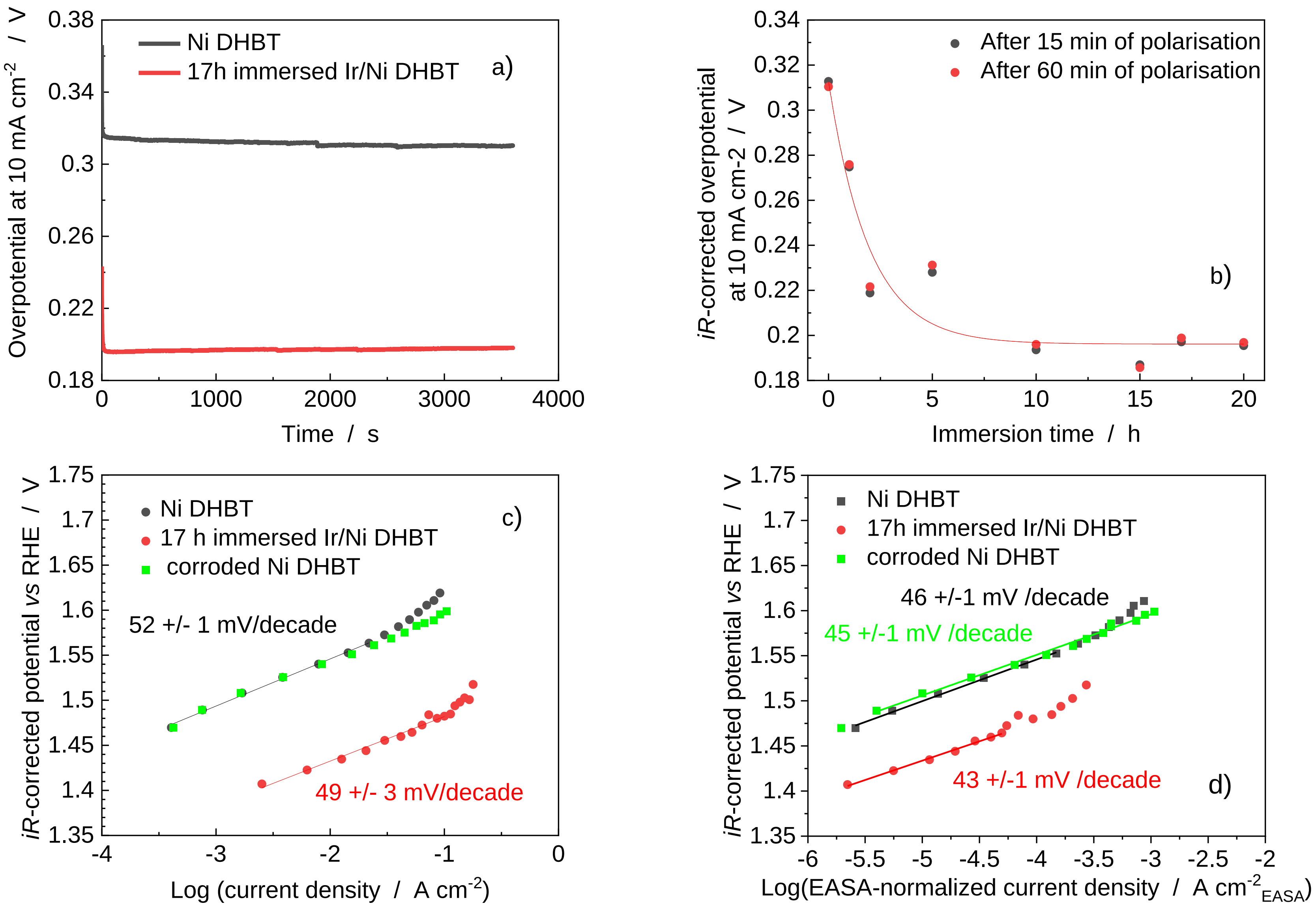

Figure 7 In a) Chronopotentiometric curves at 10 mA cm^{-2}; b) *iR*-corrected overpotentials for the OER recorded at 10 mA cm^{-2} of Ir/Ni DHBT electrodes immersed for different periods of time in 0.01 M HCl and 0.001 M K_2IrCl_6; c) Tafel plots of selected electrodes expressed as A per geometric cm^2; d) Tafel plots of selected electrodes normalized to the ECSA surface area. All OER measurements were performed in 1M KOH electrolyte.

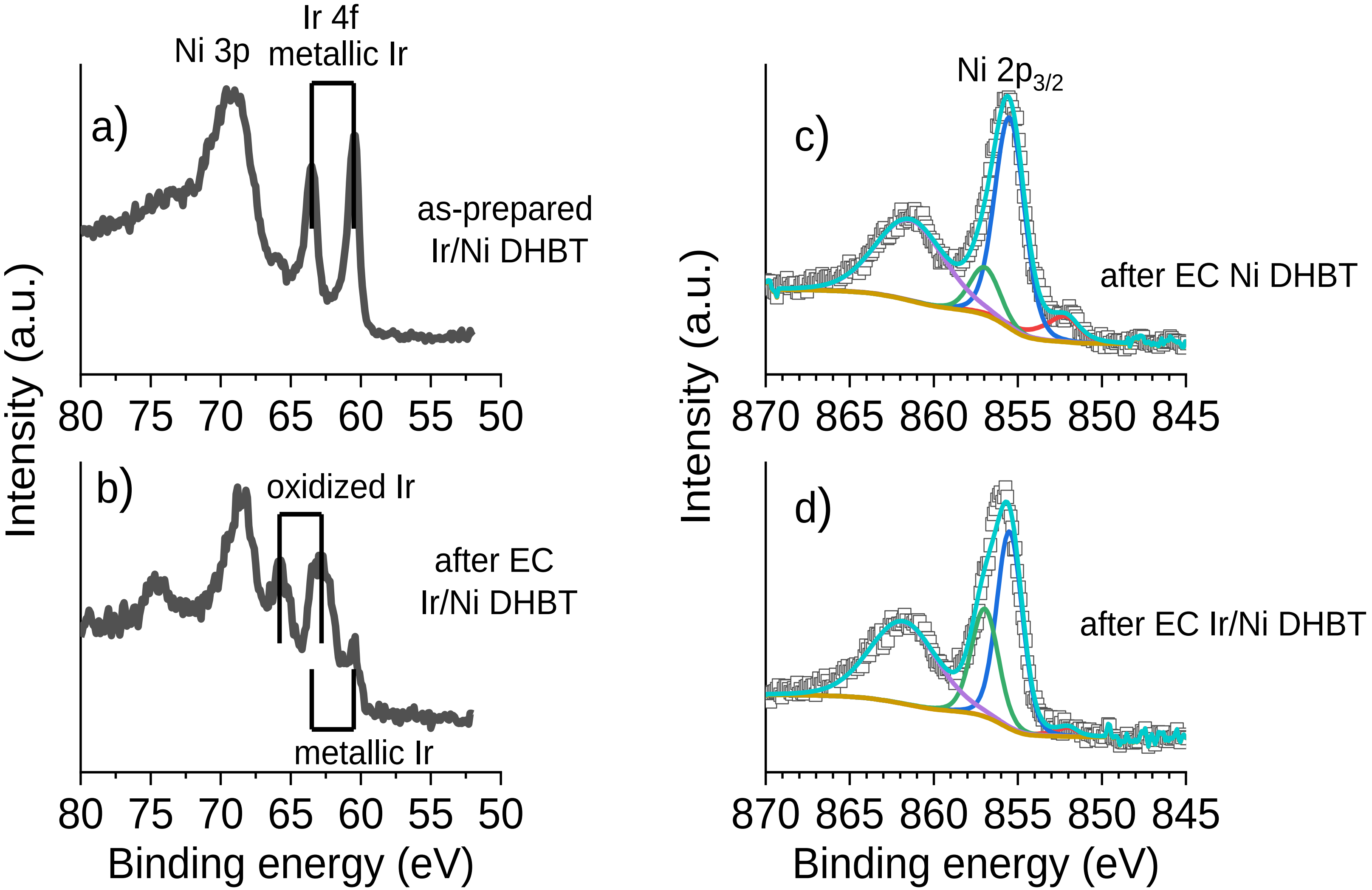

Figure 8 In (a and b), XPS data of Ir 4f and Ni 3p core levels. In (c and d), XPS data of Ni $2p_{3/2}$ core level peaks.

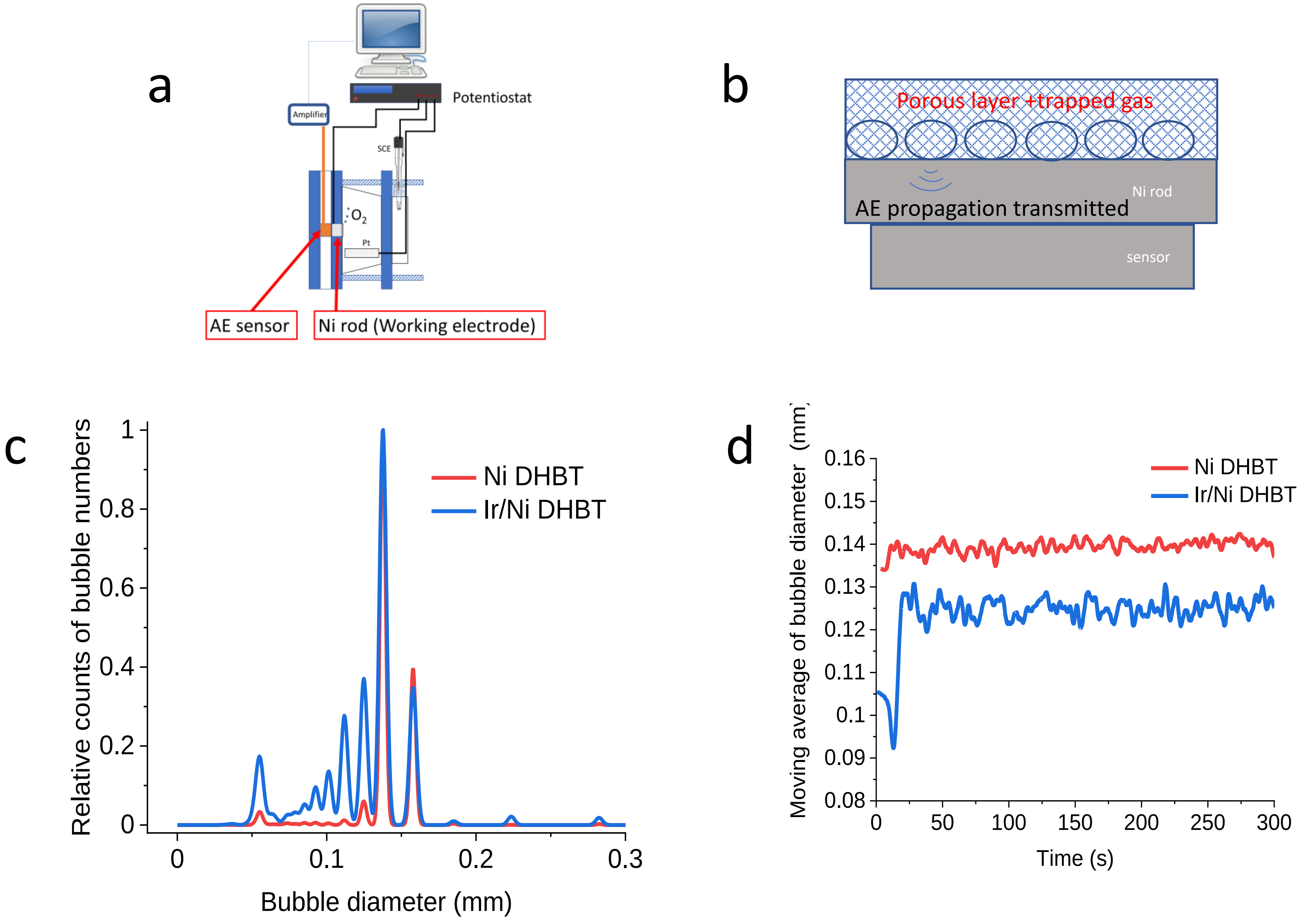

Figure 9 a) Schematic representation of the experimental setup used for the AE measurements; b) Schematic representation of the AE wave propagation of trapped bubbles; c) Bubble size distributions determined by the AE method. Measurements were performed at a current density of 6.6 mA cm^{-2} during 300s. For clarity, the distributions have been normalized to the maximum values of each plot; d) Moving averages of bubble diameter versus electrolysis time.

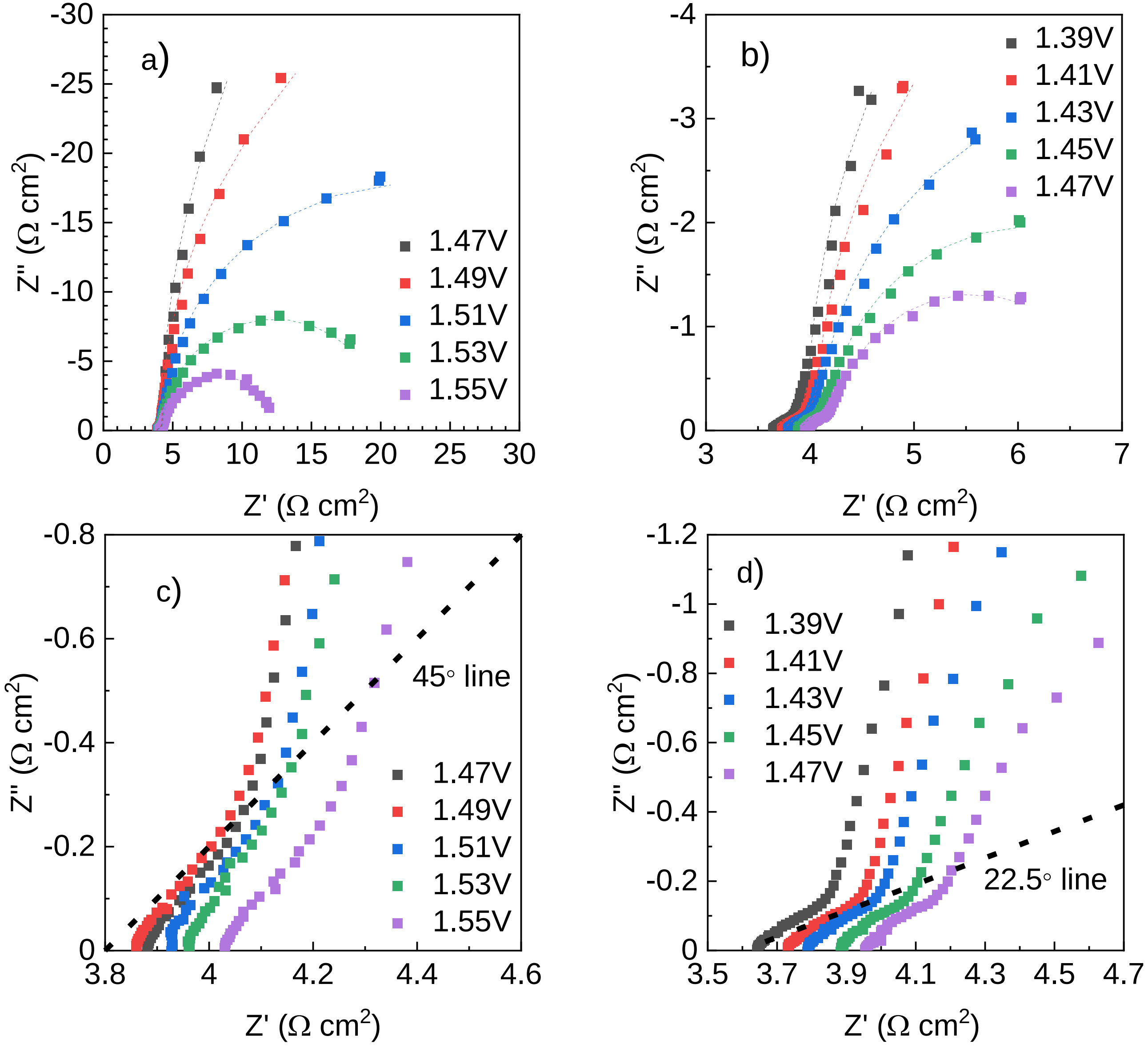

Figure 10 Measured (scattered points) and fitted (dotted lines) EIS plots on a) Ni DHBT and b) 17 h immersed Ir/Ni DHBT. The high-frequency features of Ni DHBT and 17 h immersed Ir/Ni DHBT are shown in c) and d), respectively.

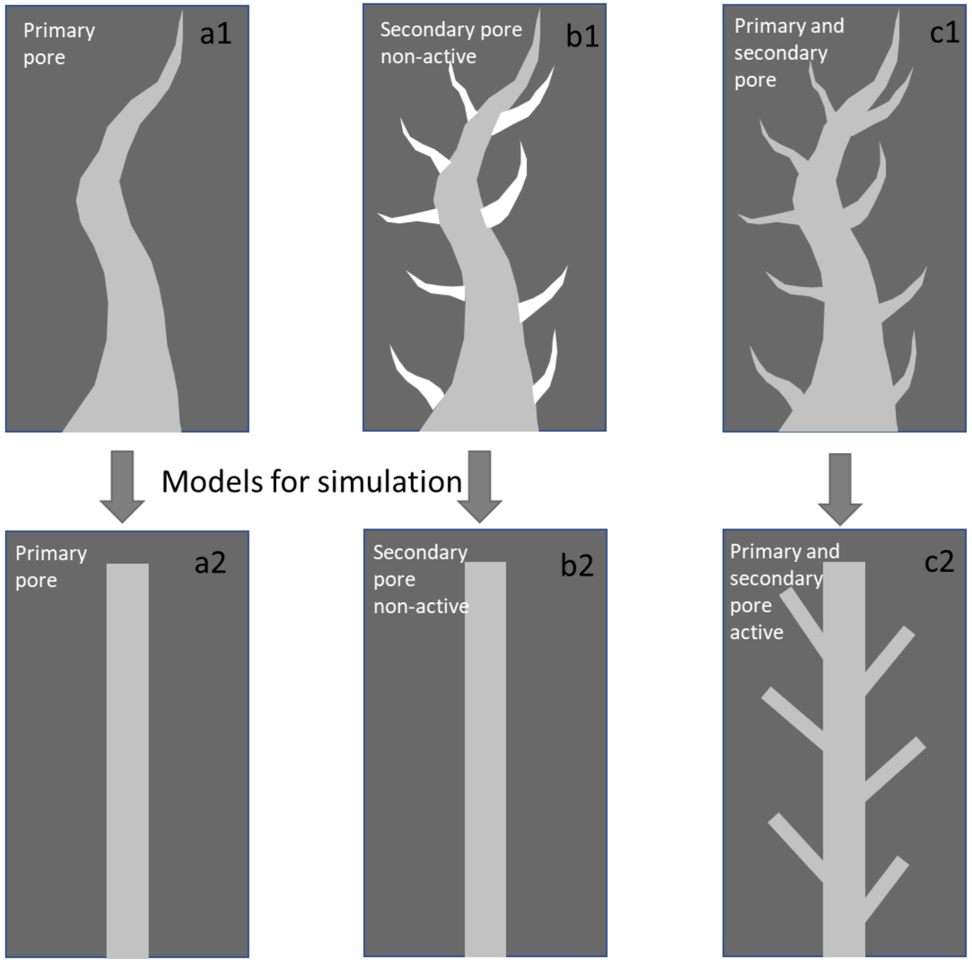

Figure 11 In a1)–c1) Schematic representations of the pores with different accessibility conditions: a) only primary pores are present; b) there primary and secondary pores are present but the secondary pores are non-active; c) primary and secondary pores are present and both are active. The gray area represents the electrochemically active region, while the white area represents non-active regions. In a2)-c2) Idealized models for EIS simulation used to represent the schematic drawings of a1)-c1), respectively.

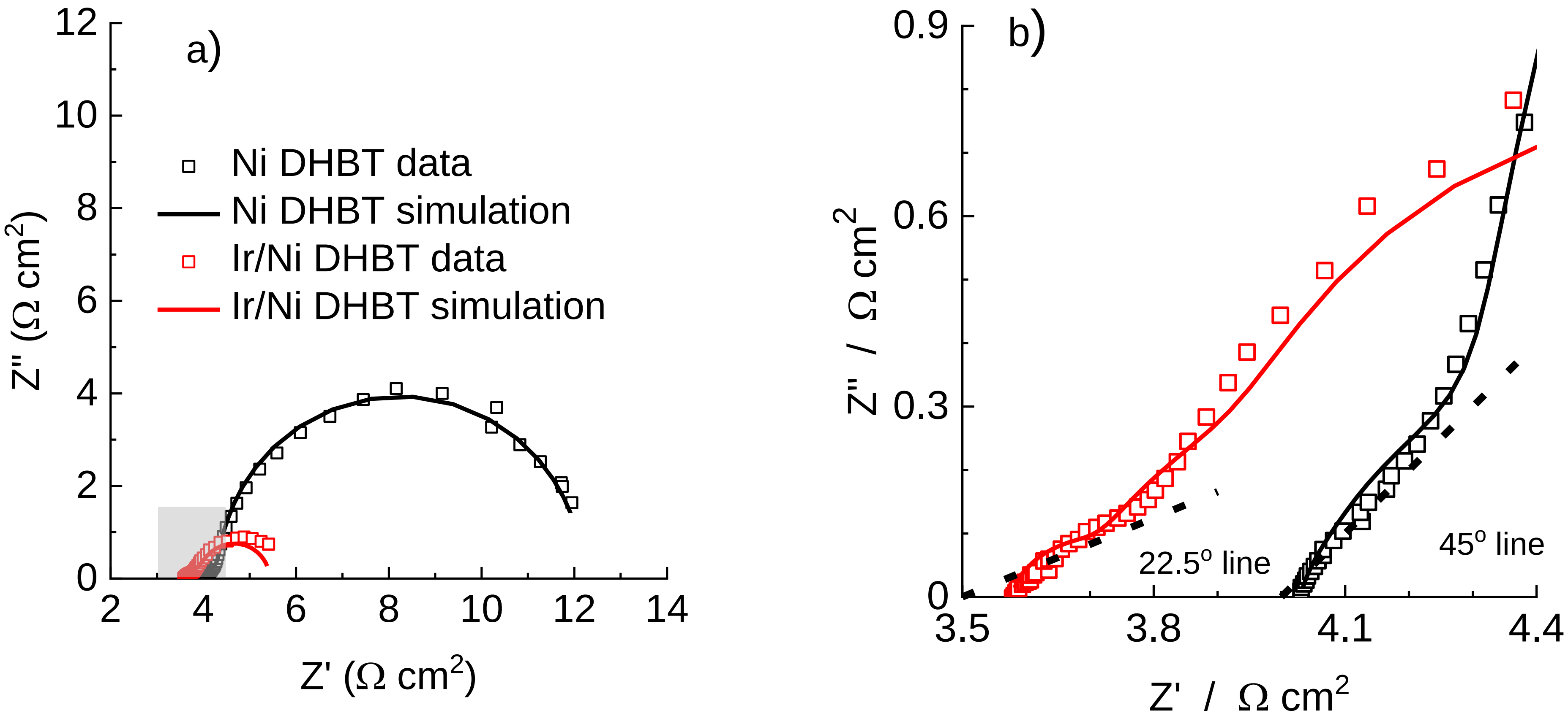

Figure 12 a) Nyquist plot of EIS measurements for Ni DHBT at 1.51V and 17h immersed Ir/Ni DHBT at 1.49V (scattered data points). The solid lines show the simulated data for Ni DHBT (black curve) and 17h immersed Ir/Ni DHBT (red curve). b) A zoom of the high frequency region (gray region in figure a). The data used for the fitted curves are shown in Table S1.

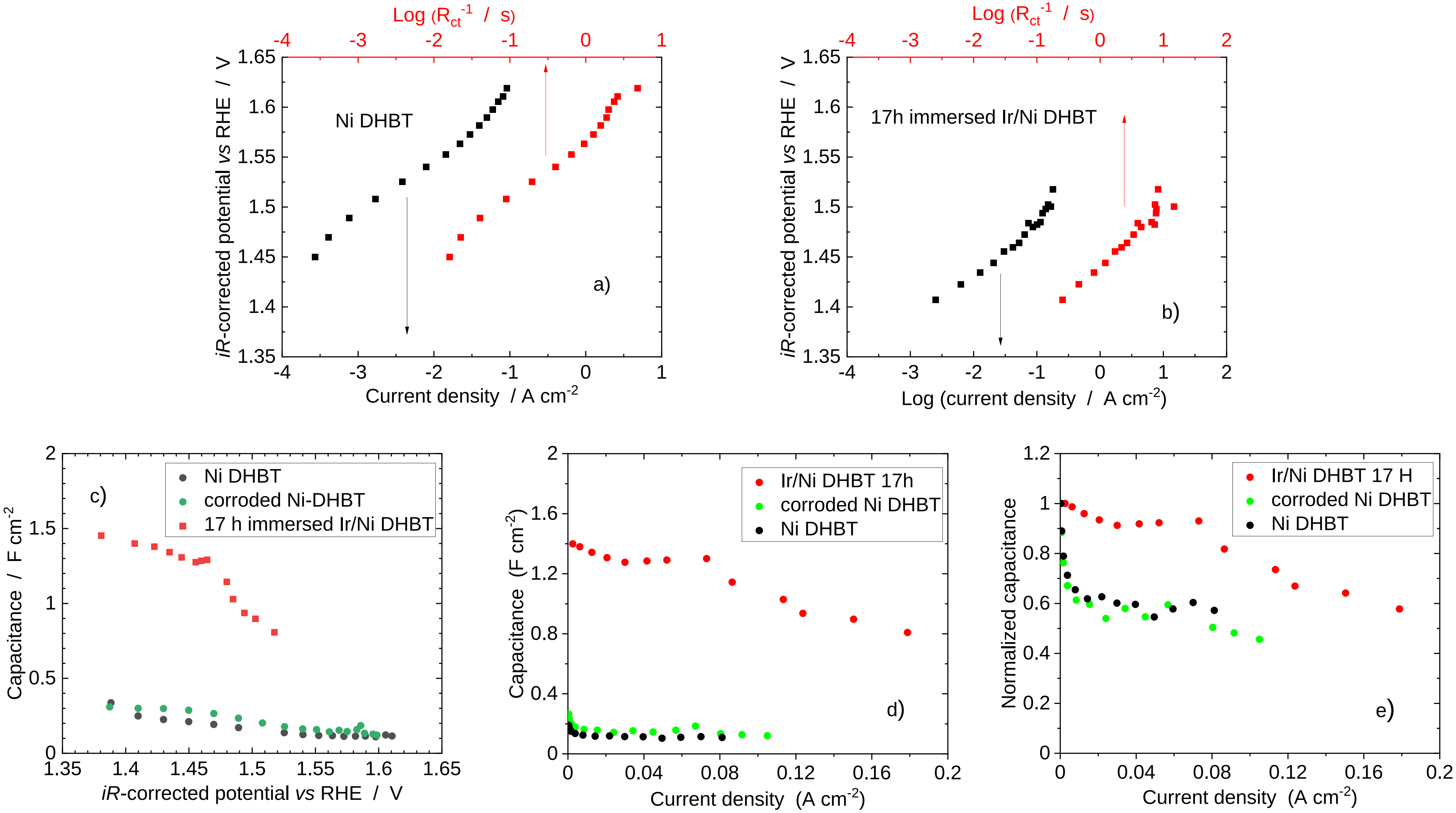

Figure 13 In a) and b), *iR*-corrected potential *versus* Log(R$^{-1}_{ct}$) determined from EIS (red data points). In a) Ni DHBT and b) 17 h immersed Ir/Ni DHBT coatings. For comparison, the corresponding Tafel plots are also given as black data points. In c), variation of the capacitance with respect to potential. In d), variation of capacitance with respect to current density. In e), variation of normalized capacitance with respect to current density.

Supporting information
The role of Ir decoration in activating multi-scale fractal surface in porous Ni for the oxygen evolution reaction

Minghui Hao[1], Birhanu Desalegn Assresahegn[1], Ahmed Abdellah[2], Lukas Miner[4],
Ahmed Al Hejami[4], Nafiseh Zaker[3], Julie Gaudet[1], Lionel Roué[1],
Gianluigi A. Botton[3], Diane Beauchemin[4], Drew C. Higgins[2]
Steven Thorpe[5], David A. Harrington[6], Daniel Guay[1 *]

[1] Institut national de la recherche scientifique (INRS), Centre Énergie, Matériaux Télécommunications, Varennes, QC J3X 1P7, Canada.

[2] Department of Chemical Engineering, McMaster University, Hamilton, Ontario L8S 4L7, Canada

[3] Department of Materials Science and Engineering, McMaster University, 1280 Main Street West Hamilton, ON L8S 4L7, Canada.

[4] Department of Chemistry, 90 Bader Lane, Queen's University, Kingston, ON K7L 3N6, Canada.

[5] Department of Materials Science and Engineering, University of Toronto, 184 College Street, Toronto, ON M5S 3E4 Canada.

[6] Department of Chemistry, University of Victoria, Victoria, BC V8W 2Y2, Canada.

* Corresponding author: daniel.guay@inrs.ca

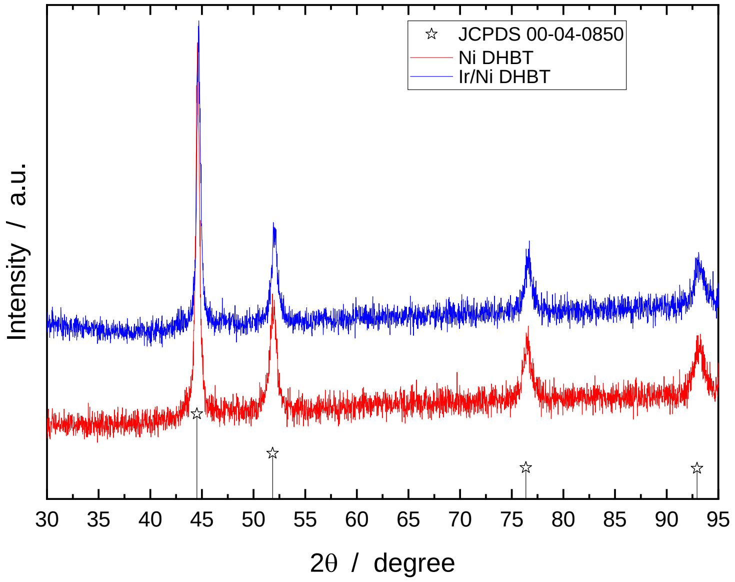

Figure S1 XRD patterns of Ni DHBT and Ir/Ni DHBT films. The stars indicate the reference pattern of Ni taken from the JCPDS card 00-04-0850.

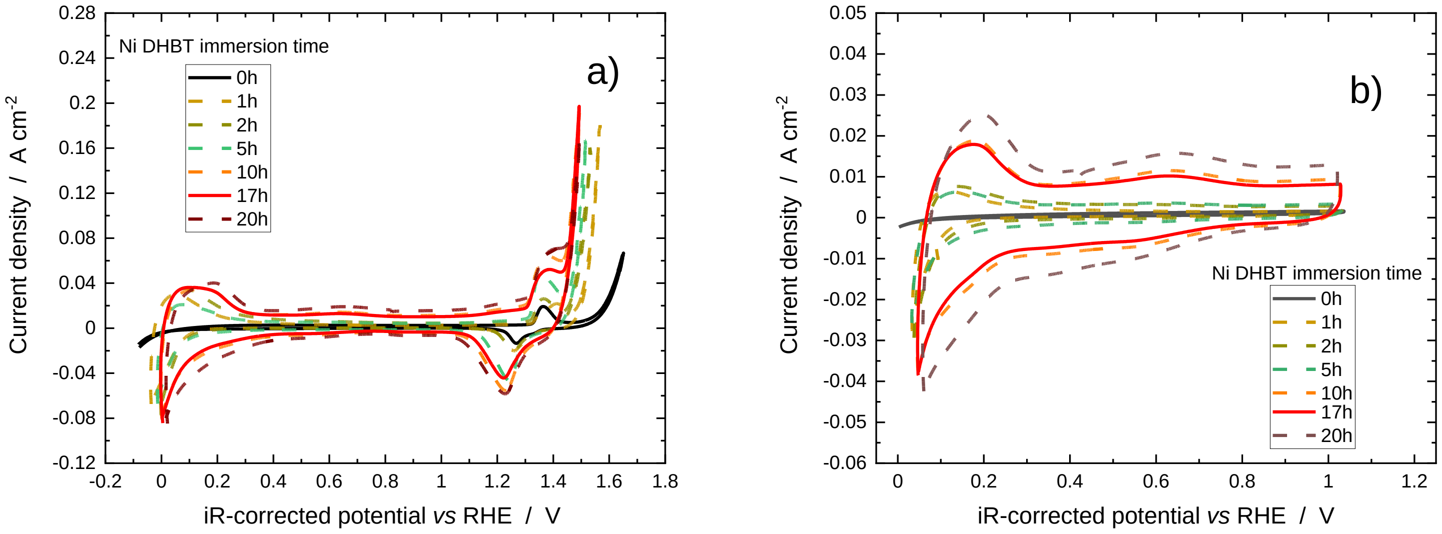

Figure S2 Cyclic voltammograms (5 mV s^{-1}) in 1 M KOH of Ir/Ni DHBT electrodes after different immersion time. In a) the potential window extends from -0.1 to 1.7 V. In b), a restricted potential window is shown.

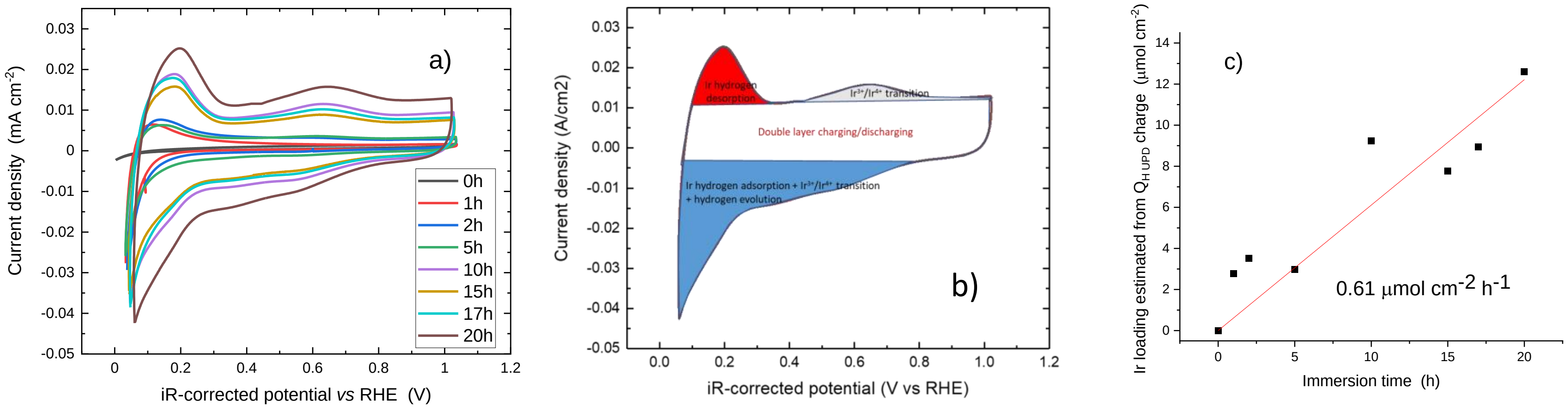

Figure S3 a) CVs of Ir/Ni DHBT before extensive electrochemical characterization in the OER region. b) Assignment of different sections in CV diagram. The white, gray, red and blue areas represent the double layer charging/discharging, the Ir(+III) to Ir(+IV) transition, hydrogen desorption and a mixture of hydrogen adsorption, the Ir(+IV) to Ir(+III) transition and hydrogen evolution, respectively. c) Variation of the estimated Ir loading determine from $Q_{H\ UPD}$ with respect to the immersion time.

$Q_{H\ UPD}$ were obtained by integrating CV curves in the hydrogen underpotential desorption region. The integration area is shown in red. According to the literature, the specific charge density for the adsorption of hydrogen on Ir is 210µC $\text{cm}^{-2}{}_{\text{Ir}}$ [1]. The atomic density of the Ir (111) surface is 1.57 x 10^{15} atoms cm^{-2} [2].

[1] Gómez, R., & Weaver, M. J. (1998). Electrochemical infrared studies of monocrystalline iridium surfaces. Part 2: Carbon monoxide and nitric oxide adsorption on Ir (110). Langmuir, 14(9), 2525-2534.
[2] Coraux, J., Plasa, T. N., Busse, C., & Michely, T. (2008). Structure of epitaxial graphene on Ir (111). New Journal of Physics, 10(4), 043033.

Calculations to estimate the Ir cluster size

The estimation of the Ir cluster size was performed as following:
The $Q_{H\,UPD}$ value of the 20h immersed Ir/Ni DHBT sample is 1.01C. The $Q_{H\,UPD}$ specific charge density of Ir density is 210 µC cm^{-2}_{Ir} [1]. So, the surface area of Ir exposed to the electrolyte is 0.48 m^2. For this sample, the total amount of Ir atoms deposited is $1.6\text{x}10^{-6}$ mol, as determined by ICP measurements, which amounts to 3.1 mg of Ir. The ratio of surface area to mass is thus 154.8 $m^2\ g^{-1}$.
As shown elsewhere [2,3], for a cuboctahedron cluster shape, the ratio between the surface area and the mass of the cluster varies with the number of atoms lying on equivalent edge, *m*.
According to them, the following equations applied:

$$S_M = \frac{(S_{c5} + S_{c7} + S_{c8} + S_{c8}) \times 10^{-18}}{\frac{\pi}{3} \times (\frac{d_M}{2} \times 10^{-7})^3 \times N_T \times \rho_M}$$

$$S_{ci} = 4\pi(\frac{d_M}{2})^2 N_{ci} \theta_{ci}$$

$$N_T = \frac{10}{3}m^3 - 5m^2 \frac{11}{3}m - 1$$

$$N_{c5} = 12$$

$$N_{c7} = 24(m-2)$$

$$N_{c8} = 6(m-2)^2$$

$$N_{c9} = 4(m-2)(m-3)$$

with S_M is the specific surface area; *m* the number of atoms lying on equivalent edge, corners atoms included; d_M the diameter of the cluster; N_T the total number of atoms; N_{ci} the total number of atoms with an *i* coordination number; S_{ci} the accessible surface area of surface atom of type N_{ci}; θ_{ci} the fraction of surface atoms of type N_{ci}; ρ_M the density of iridium.
According to our calculation that were performed with Matlab, a cuboctahedron cluster with 2869 Ir atoms and a diameter of 4.3 nm has a ratio of surface area to mass ratio of 154.8 $m^2\ g^{-1}$.
Accordingly, we have inferred that Ir atoms exist at the surface of the Ir/Ni DHBT electrode as 4.3 nm diameter clusters, and that there must have a total of 4.7 x 10^{15} of such clusters.

[1] Gómez, R., & Weaver, M. J. (1998). Electrochemical infrared studies of monocrystalline iridium surfaces. Part 2: Carbon monoxide and nitric oxide adsorption on Ir (110). Langmuir, 14(9), 2525-2534.
[2] Drault, F., Comminges, C., Can, F., Pirault-Roy, L., Epron, F., & Le Valant, A. (2018). Palladium, Iridium, and Rhodium supported catalysts: Predictive H2 chemisorption by statistical cuboctahedron clusters model. Materials, 11(5), 819.
[3] Le Valant, A., Comminges, C., Can, F., Thomas, K., Houalla, M., & Epron, F. (2016). Platinum supported catalysts: Predictive CO and H2 chemisorption by a statistical cuboctahedron cluster model. The Journal of Physical Chemistry C, 120(46), 26374-26385.

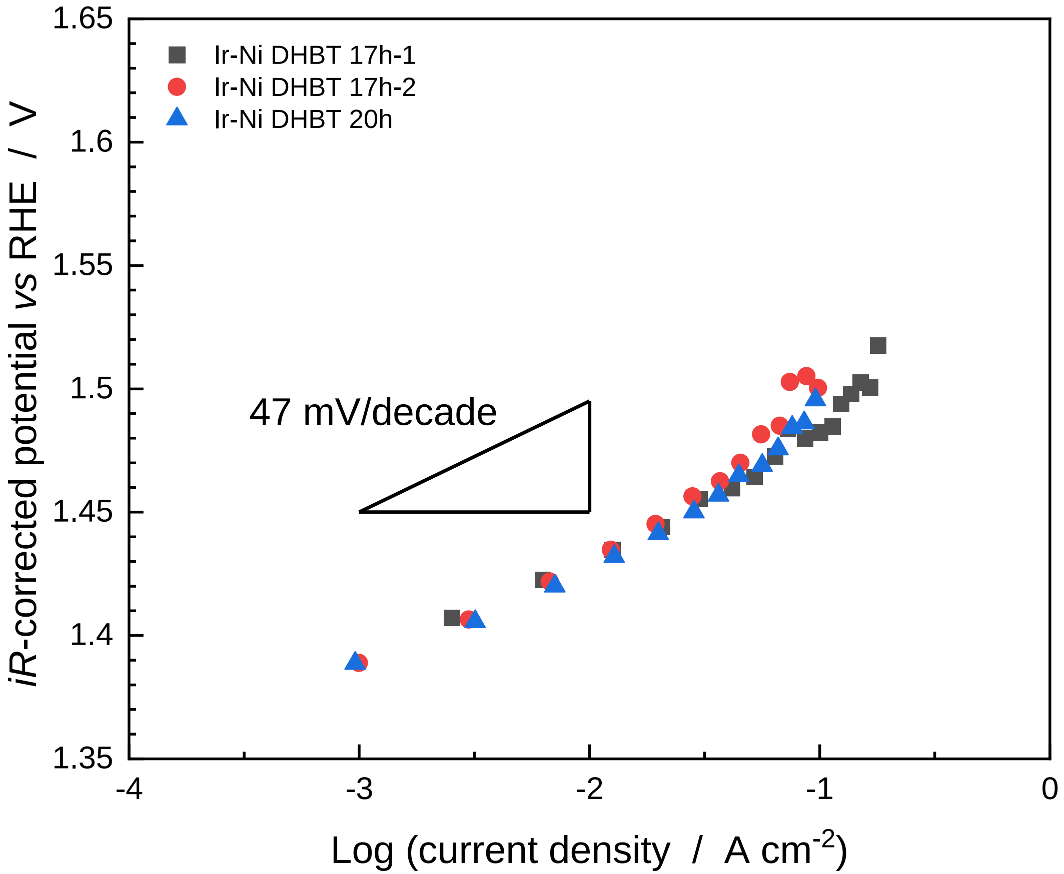

Figure S4 Tafel plots of replicates of the best performing electrodes taken in 1M KOH. Ir/Ni DHBT 17h-1 and Ir/Ni DHBT 17h-2 corresponds to two replicates of the Ni DHBT electrodes that were immersed 17 h in 0.01 M HCl and 0.001 M K_2IrCl_6.

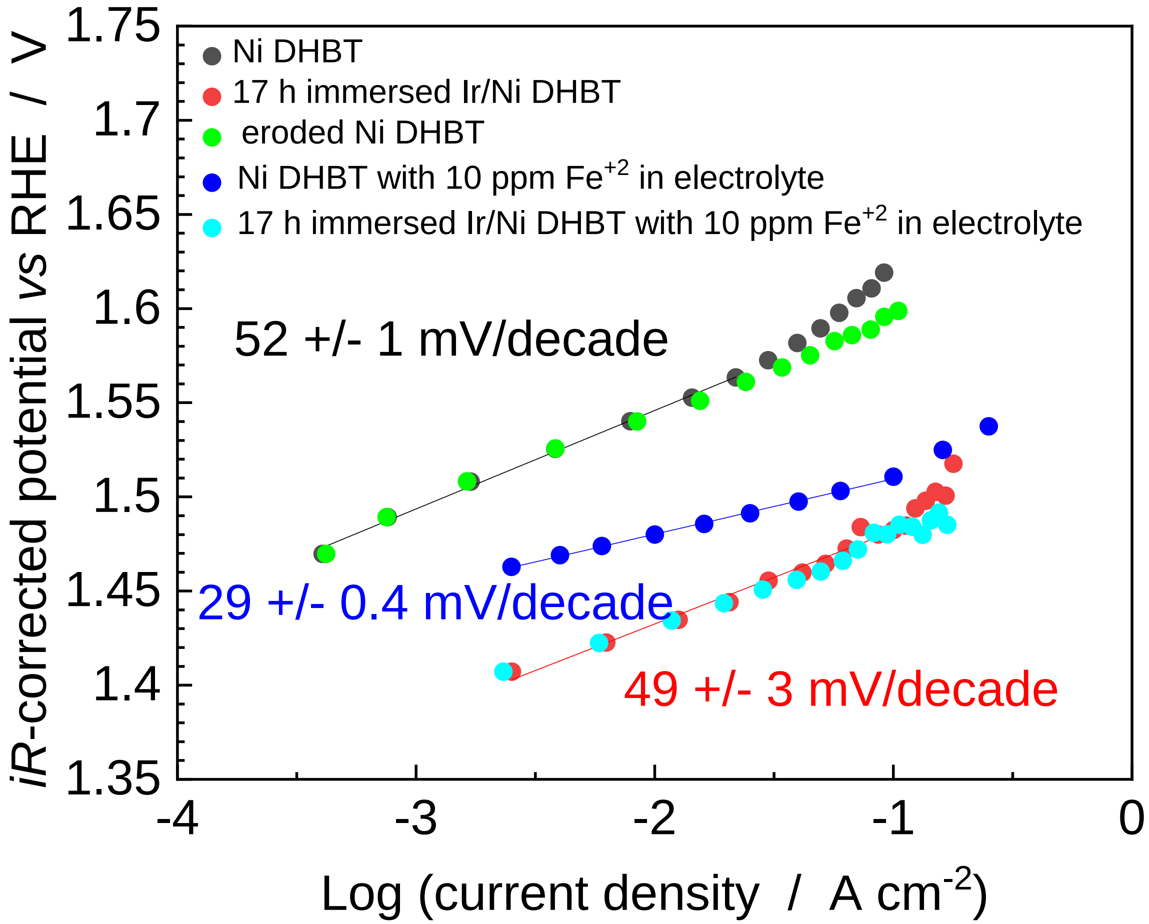

Figure S5 Tafel plots of selected electrodes in 1M KOH. In some cases, the 1M KOH electrolyte was spiked with 10 ppm Fe ($FeCl_2 \cdot 6H_2O$).

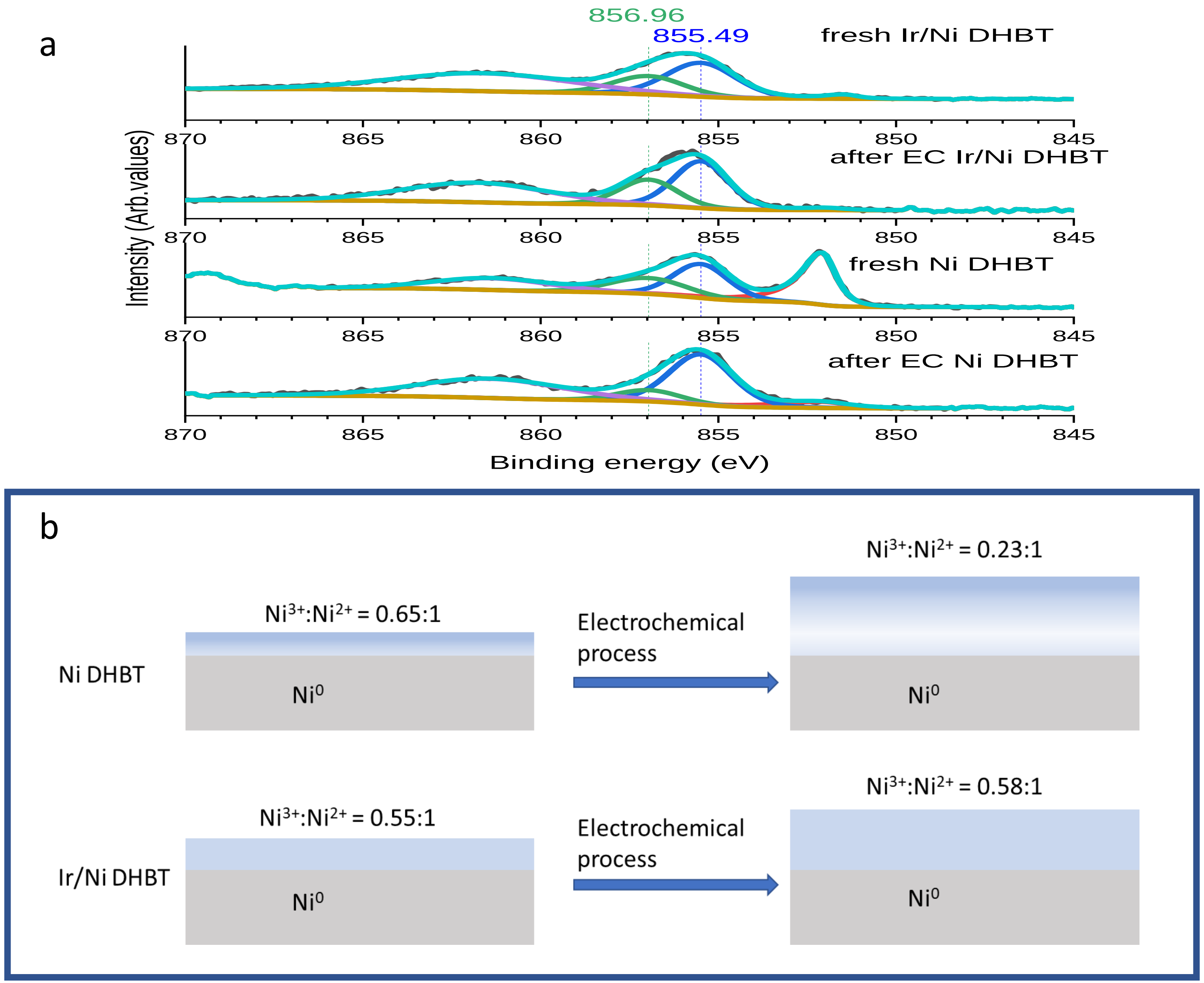

Figure S6 In a) XPS Ni 2p deconvolutions in the $2p_{3/2}$ region with Ni^0 at 852.15 eV, Ni^{2+} at 855.49 eV and Ni^{3+} at 856.96 eV peaks; In b) schematic presentation of Ni^{3+}/Ni^{2+} ratios on different samples.

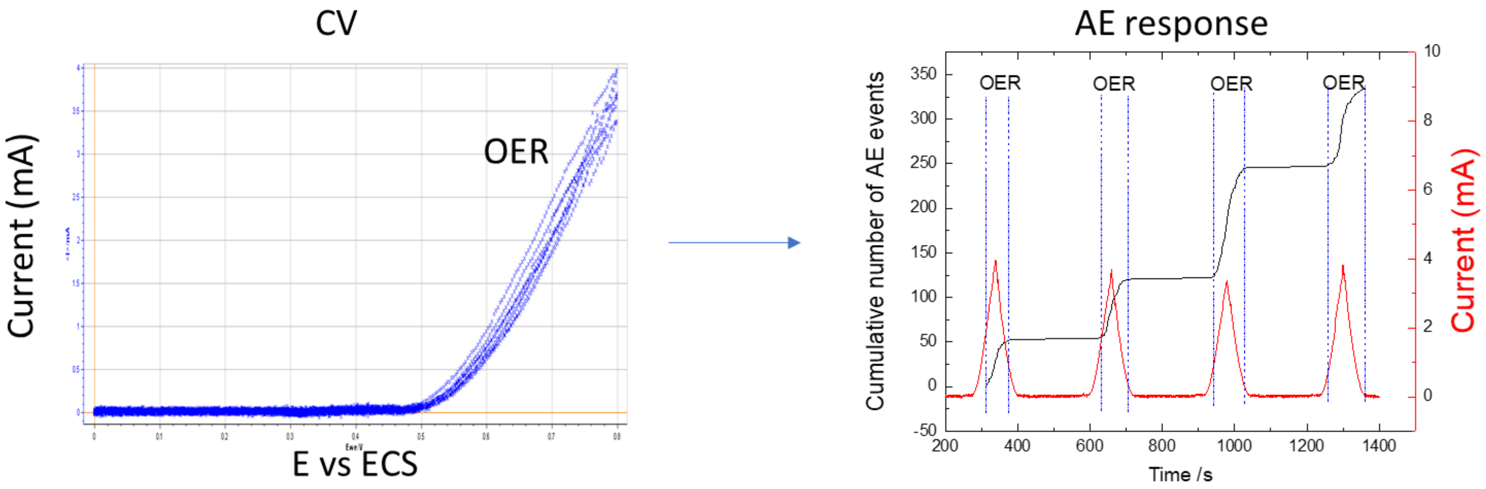

Figure S7 In (a), CVs of a Ni plate taken in 1M KOH at 5 mV s^{-1}. In (b), variation of current and cumulative number of AE events as a function of time.

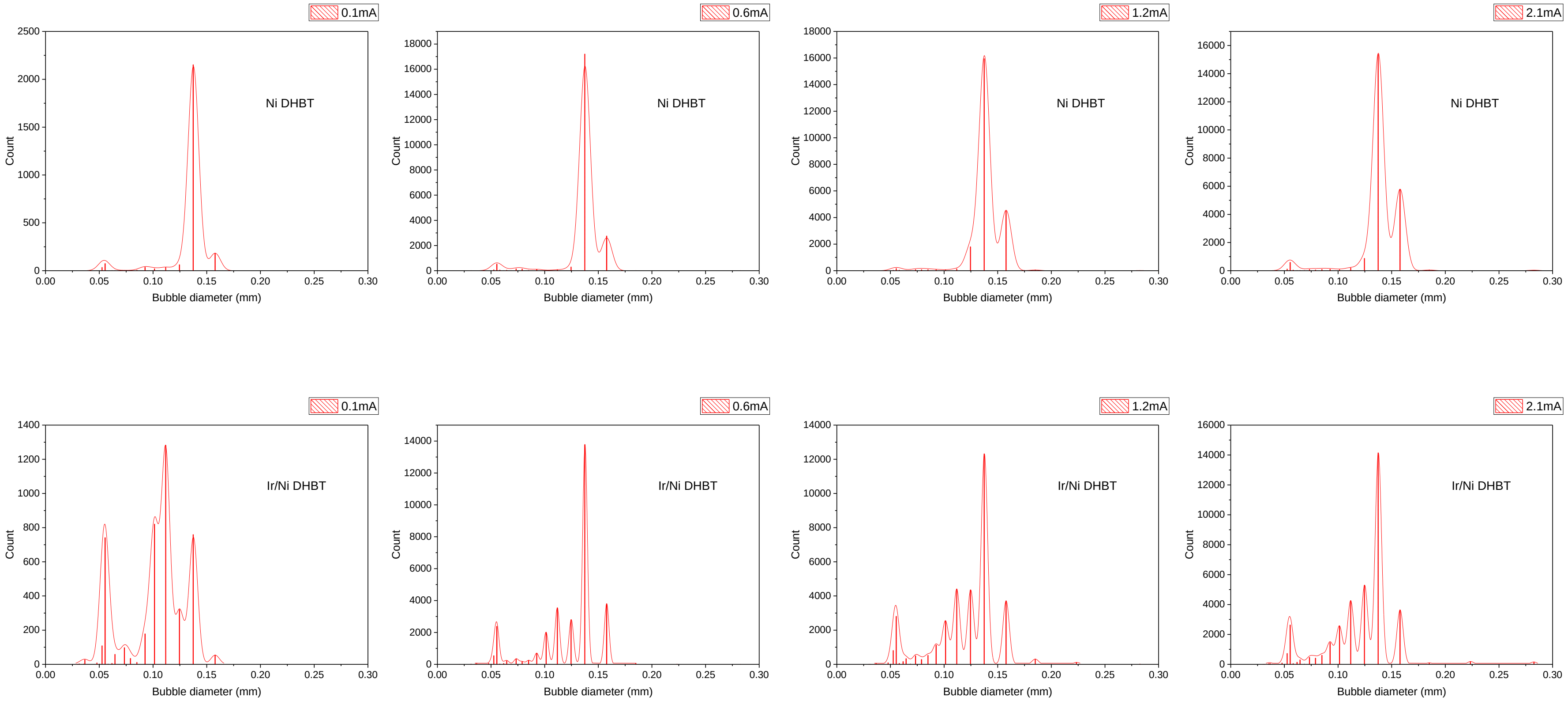

Figure S8 Bubble size distributions determined by the AE method for a) to d) Ni DHBT, and e to h) Ir/Ni DHBT at current density of 0.3 mA/cm^2 (first column), 1.9 mA/cm^2 (second column), 3.8 mA/cm^2 (third column), and 6.6 mA/cm^2 (fourth column).

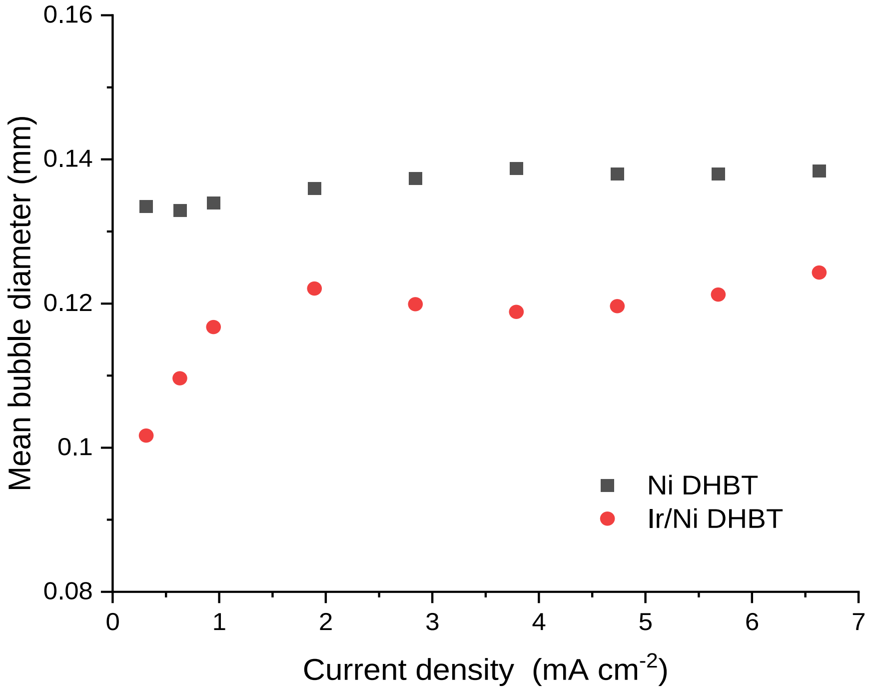

Figure S9 Average bubble diameter measured by AE at different current densities for Ni DHBT and Ir/Ni DHBT electrode.

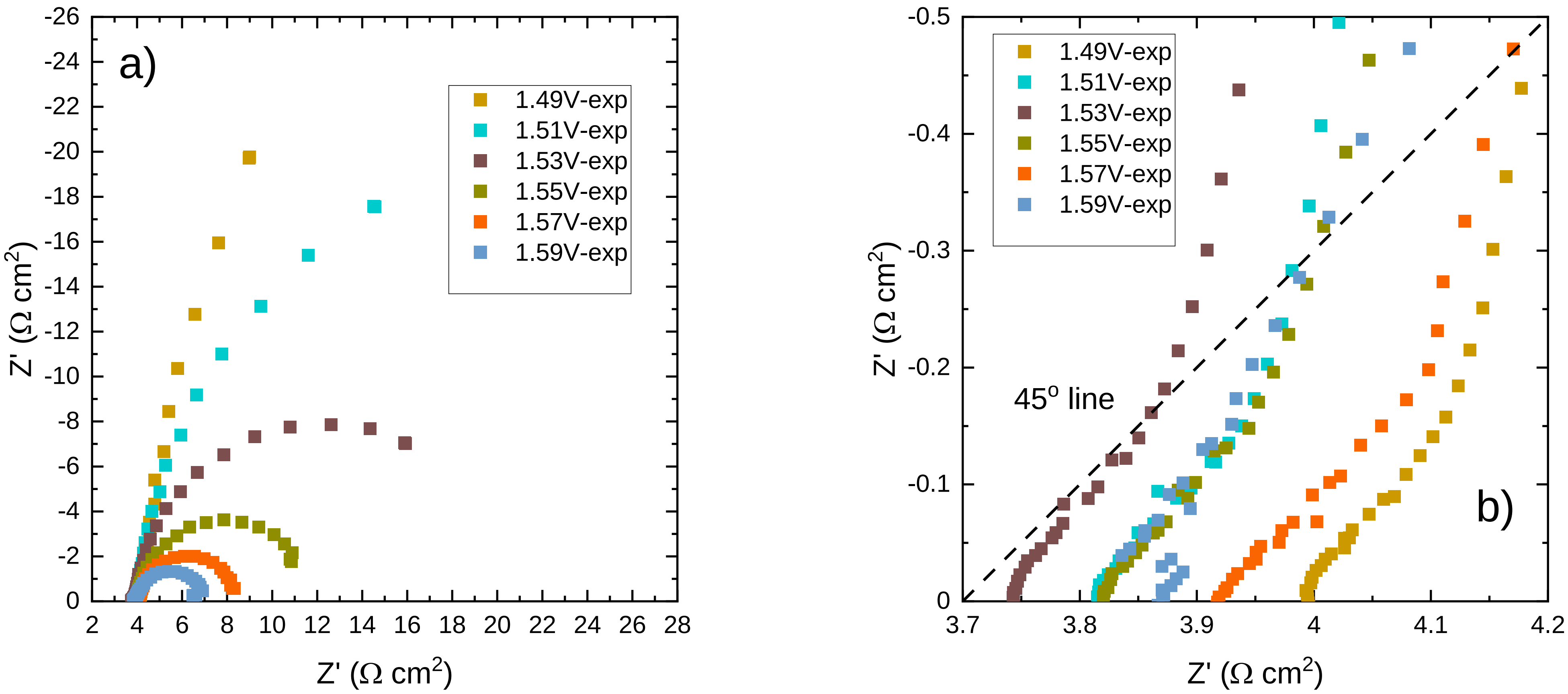

Figure S10 EIS plots of eroded Ni DHBT electrodes. The experimental data are given as scattered data points. The same data are shown at different scales in a) and b).

Table S1 : The parameters used for the EIS simulation of Ni DHBT and Ir/Ni DHBT

		Rs	Z_{flat}	r_1	r_2	X_1	X_2	$n_{pore,1}$	$n_{pore,2}$	$R_{\Omega,pore1}$	$R_{\Omega,pore2}$	Rct*	Cdl*	ξ	ρ
Ni DHBT	Formula		$1/[(\frac{1}{R_{ct}^*}+i\omega C_{dl}^*)\text{x}2.5S_1]$							ρ/s_1					
	value	4.02Ω		11μm	0	95μm	0	$4.2\text{x}10^6$ cm^{-2}	-		-	586Ω cm^2	390μF cm^{-2}	0	586 Ω cm
Ir/Ni DHBT	Formula		$1/[(\frac{1}{R_{ct}^*}+i\omega C_{dl}^*)\text{x}2.5S_1]$		$0.3r_1$		$0.3X_1$		$1/s_2$	ρ/s_1	ρ/s_2				
	value	4.02Ω		11μm		95μm		$4.2\text{x}10^6$ cm^{-2}				586Ω cm^2	390μF cm^{-2}	0.3	586 Ω cm

* S1 is the total intersecting surface of primary pores, s1 and s2 are the intersecting surface of primary pore and secondary pore respectively. ρ is the resistivity of electrolyte (Ω cm).

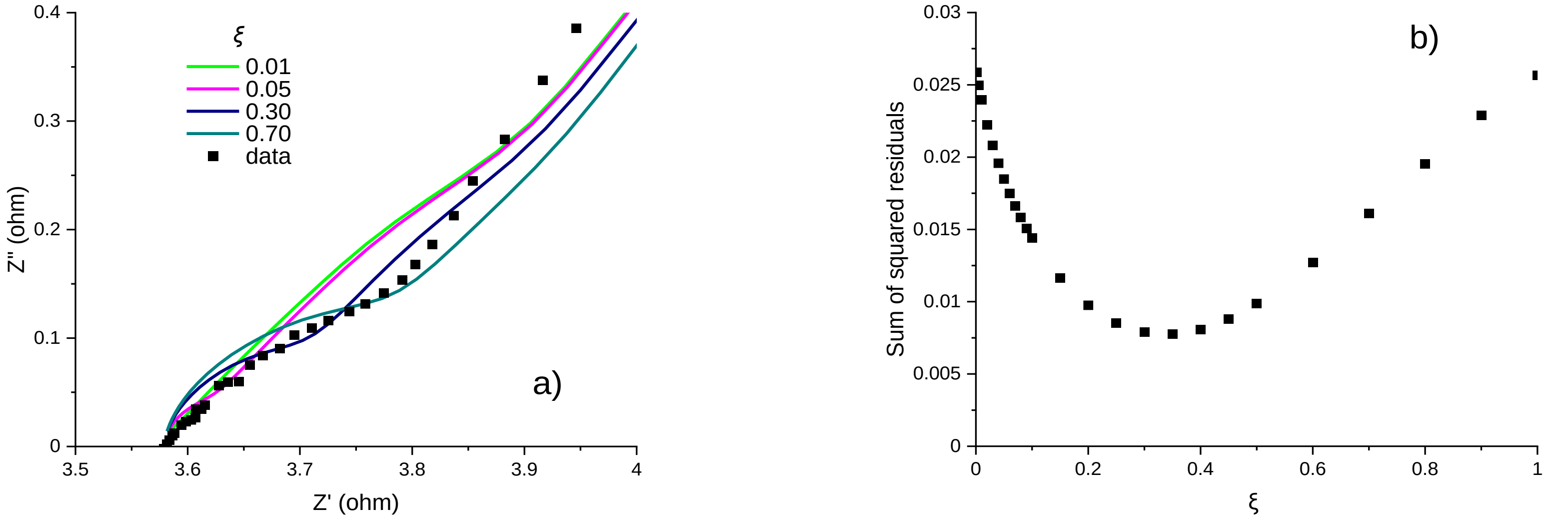

Figure S11 In a), simulations of EIS data for Ir/Ni DHBT in the high-frequency region using different values of ξ. In b), sum of squared residuals as a function of ξ. It was shown elsewhere that the Ni DHBT substrate has a fractal surface. So, in each case, the EIS simulation were obtained by assuming that the secondary pores occupied of ξ*100 % of the primary pore wall area, that the diameter of the secondary pores was ξ*100 % of the primary pore diameter, and that the length of the secondary pores was ξ*100 % of the primary pore length.